

AD-A265 877



2

ARMY RESEARCH LABORATORY



## Modeling the Impact Behavior of AD85 Ceramic Under Multi-Axial Loading

A. M. Rajendran

ARL-TR-137

May 1993



Approved for public release; distribution unlimited.

93-13480



98

171

The findings in this report are not to be construed as an official Department of the Army position unless so designated by other authorized documents.

Citation of manufacturer's or trade names does not constitute an official endorsement or approval of the use thereof.

Destroy this report when it is no longer needed. Do not return it to the originator.

REPORT DOCUMENTATION PAGE			Form Approved OMB No. 0704-0188	
<small>Public reporting burden for this collection of information is estimated to average 1 hour per response, including the time for reviewing instructions, searching existing data sources, gathering and maintaining the data needed, and completing and reviewing the collection of information. Send comments regarding this burden estimate or any other aspect of this collection of information, including suggestions for reducing this burden, to Washington Headquarters Services, Directorate for Information Operations and Reports, 1215 Jefferson Davis Highway, Suite 1204, Arlington, VA 22202-4302, and to the Office of Management and Budget, Paperwork Reduction Project (0704-0188), Washington, DC 20503.</small>				
1. AGENCY USE ONLY (Leave blank)		2. REPORT DATE May 1993		3. REPORT TYPE AND DATES COVERED Final Report
4. TITLE AND SUBTITLE Modeling the Impact Behavior of AD85 Ceramic Under Multi-Axial Loading			5. FUNDING NUMBERS	
6. AUTHOR(S) A. M. Rajendran				
7. PERFORMING ORGANIZATION NAME(S) AND ADDRESS(ES) U.S. Army Research Laboratory Watertown, MA 02172-0001 ATTN: AMSRL-MA-DA			8. PERFORMING ORGANIZATION REPORT NUMBER ARI-TR-137	
9. SPONSORING/MONITORING AGENCY NAME(S) AND ADDRESS(ES) U.S. Army Research Laboratory 2800 Powder Mill Road Adelphi, MD 20783-1145			10. SPONSORING/MONITORING AGENCY REPORT NUMBER	
11. SUPPLEMENTARY NOTES				
12a. DISTRIBUTION/AVAILABILITY STATEMENT Approved for public release; distribution unlimited.			12b. DISTRIBUTION CODE	
13. ABSTRACT (Maximum 200 words)  This report presents an advanced constitutive model to describe the complex behavior of ceramic materials under impact loading conditions. The governing equations utilize a set of microphysically based constitutive relationships to model deformation and damage processes in a ceramic. The total strain is decomposed into elastic, plastic, and microcracking components. The model parameters for AD85 ceramic were determined using the data from split Hopkinson bar (SHB) and bar-on-bar experiments under uniaxial stress state and plate impact experiment under uniaxial strain state. To further validate the generality of the model parameters, modeling of a diagnostic ballistic experiment in which a steel projectile impacted an AD85 ceramic front-faced thick aluminum plate was considered. In this experiment, stress histories were measured in the target by embedded manganin and carbon stress gauges. The results from the numerical simulations of the ballistic experiment using a shock wave propagation based finite element code successfully matched the measured stress history.				
14. SUBJECT TERMS Impact, High strain rate, Ceramic, Modeling, Damage, Microcracks, Hydrocode			15. NUMBER OF PAGES 44	
			16. PRICE CODE	
17. SECURITY CLASSIFICATION OF REPORT Unclassified	18. SECURITY CLASSIFICATION OF THIS PAGE Unclassified	19. SECURITY CLASSIFICATION OF ABSTRACT Unclassified	20. LIMITATION OF ABSTRACT UL	

## Contents

	Page
Introduction . . . . .	1
Rajendran-Grove Ceramic Model . . . . .	3
Constitutive Relationships . . . . .	4
Definition of Damage . . . . .	5
Microcrack Nucleation . . . . .	6
Damage Growth Model . . . . .	7
Model Parameters Determination . . . . .	8
Modeling the Ballistic Impact Pressure Measurements . . . . .	11
The Ballistic Experiment . . . . .	12
Simulation Details . . . . .	13
Results and Analyses . . . . .	14
Summary and Conclusions . . . . .	
Summary . . . . .	28
Conclusions . . . . .	29
Acknowledgments . . . . .	29
References . . . . .	30
Appendix . . . . .	
Degraded Moduli Expressions . . . . .	32

## Figures

1. A comparison between model and measured stress history in a plate impact experiment on AD85 target . . . . .	10
2. A comparison between model and measured stress history in an AD85 bar-on-bar experiment . . . . .	10
3. A schematic of the instrumented ballistic experiment . . . . .	11
4. Manganin gauge measured stress histories in a ballistic experiment . . . . .	12
5. The finite element mesh for the ballistic experiment . . . . .	15
6. A close-up view of the finite element mesh near the impact region . . . . .	16
7. Effects of mesh on stress history . . . . .	17
8. Effects of time step on stress history . . . . .	18

9.	A comparison between bottom gauge data and Case E. The ceramic behavior is assumed elastic . . . . .	18
10.	A comparison between top gauge data and Case E. The ceramic behavior is assumed elastic . . . . .	19
11.	A comparison between bottom gauge data and Case EP. The ceramic behavior is assumed elastic-plastic (no cracking) . . . . .	20
12.	A comparison between top gauge data and Case EP. The ceramic behavior is assumed elastic-plastic (no cracking) . . . . .	21
13.	A comparison between bottom gauge data and Case EC. The ceramic behavior is assumed elastic cracking (no plastic flow) . . . . .	22
14.	A comparison between the ceramic model (with tensile $n_1 = 1$ ) and bottom gauge data . . . . .	23
15.	The microcracking damage shade plot at time 4 microseconds . . . . .	24
16.	The microcracking damage shade plot at time 8 microseconds . . . . .	24
17.	A comparison between top gauge data and the ceramic model (with tensile $n_1 = 0.1$ ) . . . . .	25
18.	A comparison between the Rajendran-Grove ceramic model (with tensile $n_1 = 0.1$ ) and bottom gauge data . . . . .	26
19.	A comparison between stress histories for the cases with and without interface slide lines and the bottom gauge data . . . . .	27

### Tables

1.	Model constants for AD85 ceramic . . . . .	9
2.	Projectile dimensions and materials . . . . .	13
3.	Target dimensions . . . . .	13
4.	Material constants for isodamp and AD85 . . . . .	14

Accession For		D-11	
Name	Project		
Organization	Contract		
Justification	Priority		
By	Date	Availability Codes	
Approved	Specialist		
Dist.	A-1		

## Introduction

Advanced armor design calculations to understand and evaluate the performance of armor elements often employ hydrocodes (shock wave propagation based finite element/difference numerical codes). For realistic design calculations using hydrocodes, the impact behavior of armor materials must be accurately described with physically based constitutive/failure models. This is especially true for advanced armor materials such as ceramics. Since constitutive and damage models for ceramics are rarely available in hydrocodes, several preliminary versions of new models have been implemented into different hydrocodes. Most of these new models are in the process of being validated and evaluated.

The high velocity impact behavior of ceramics is dominated by stiffness loss. The inelastic deformations are due to microcracking and dislocation generated microplastic flows. In the microcracking approach, the (strain) response of a single crack to an externally applied stress field is calculated using the appropriate stress-free boundary conditions on the crack surfaces. The derived strain components include the effects of microcracks in a brittle material through a crack density parameter. However, the bulk material itself is treated as a continuum so that all the stress-strain equations can be derived under the continuum mechanics based theoretical framework. The microplasticity in a brittle solid is often attributed to the dislocation motions in the vicinity of microflaw tip regions. In brittle solids, large scale grain distortions are usually absent.

Unlike metals, most ceramics pulverize upon high velocity impact thereby eliminating the possibility of any post-impact microscopic measurement/analysis. The American Physical Society conference proceedings [1] report several microstructural studies on ceramic targets recovered under low velocity (below Hugoniot Elastic Limit) impact conditions. The microscopic evaluations of the recovered targets provide useful information on microcrack initiation under compressive loading conditions. Since the effects of nucleation and growth of microcracks on the constitutive behaviors of ceramics are important in the modeling, the low velocity impact studies are often important.

In the absence of any post-impact measurements on most ceramic targets, the ceramic behavior under high velocity (above Hugoniot Elastic Limit) impact is usually evaluated through stress and velocity measurements at the back of the target plates. These measurements yield dynamic properties such as the Hugoniot stress and spall strength. In these experiments, the ceramic targets are backed by plastic materials such as plexiglass and lithium fluoride. Rajendran and Cook [2] conducted an in-depth literature review of impact behavior of ceramics and reported the need for ceramic constitutive and damage models in advanced hydrocodes. Subsequently, during 1988 through 1992 a few new models have been developed and reported to describe the impact behavior of ceramic materials.

Johnson and Holmquist [3] considered a phenomenological approach in their model formulation. The strength variation with respect to pressure, strain rate, and damage was modeled using a set of empirical relationships. In their model, the strains are due to elastic and plastic deformations. No attempt was made to characterize the inelastic deformation due to microcrack opening and/or sliding.

Damage is defined as the ratio of accumulated strain and a fracture strain. This definition of damage is similar to the metal fracture model of Johnson and Cook [4]. Johnson and Holmquist included data from both static and dynamic tests under uniaxial compressive loading in their model parameters reduction scheme.

Steinberg [5] adopted his metal model equations for high pressure dynamic loading to describe the impact behavior of ceramics. In this model, the compressive yield strength and shear modulus are varied with respect to pressure and temperature. In addition, the yield strength is multiplied by the normalized shear modulus. The strain rate effects are introduced through a simple power law. There are two constants in the power law. The two constants are determined using the fracture toughness dependent relationship of Grady [6] and the quasi-static and split Hopkinson bar (SHB) data. However, the tensile damage is modeled through the Cochran and Banner spall model [7]. Steinberg's model assumes no compressive damage in the ceramics. Steinberg successfully reproduced the measured velocity histories from plate impact experiments for various ceramic materials.

Addessio and Johnson [8] presented a microphysical model to describe the complex behavior of ceramics. In their model, the inelastic strain is assumed to be due to microcracking of the ceramics. They modeled crack opening under tensile pressure loading and crack sliding under compressive pressure. The plastic flow or pore collapse effects are not built into the model; however, an extension of this model to include such effects is feasible. Damage is described by a crack density parameter. The damage evolution is described through energy-balance based failure surfaces. Addessio and Johnson introduced arbitrary modifications to the model and successfully reproduced the measured velocity histories for several ceramics under one-dimensional strain conditions. This three-dimensional, continuum mechanics model has not been validated under any other stress-strain states.

Rajendran and Kroupa [9] presented a ceramic model in which they assumed an elastic-viscoplastic behavior for compressive loading and microcracking behavior for tensile loading. In general, attributing the inelastic strains entirely to dislocation-based plastic flow is not appropriate for brittle ceramics. However, this model may be useful to describe crushing/pulverization of the ceramic materials under high pressures (>10 GPa) and dominantly tensile damage. The tensile cracking is described using the rock fragmentation relationships derived by Grady and Kipp [10]. Since it is a fragmentation based tensile fracture model, the model's applicability is limited and any extension of this model includes the less appealing plastic work or plastic strain-based compressive damage description.

Recently, Rajendran [11] reported a continuum mechanics based, three-dimensional constitutive model to describe the complex behaviors of ceramic materials. This model [12 through 14] is based on microcrack nucleation and growth, as well as pore collapse mechanisms. Damage is defined in terms of an average crack density and is treated as an internal state variable. To keep the model formulation relatively simple, the damage nucleation is not modeled and the microcracks are assumed to be present prior to loading. This scalar damage model incorporates the effects of different damage processes under tension and compression using fracture mechanics based fracture criteria.

The stiffness reduction due to microcracking is modeled using Margolin's [15] analytically derived damaged moduli. The damage evolution under both tensile and compressive loadings is formulated based on a generalized Griffith criterion. The pore collapse effects are modeled using viscoplastic equations derived from Gurson's pressure dependent yield function [16]. This model decomposes total strains into elastic and dislocation motion-controlled plastic components. The elastic strains are further decomposed into average strains in the intact matrix material and strains due to crack opening/sliding. The strain rate and pressure effects on strength are implicitly described by the degraded elastic moduli based stress-strain equations. Rajendran and Grove [14] and Grove, et al. [12] successfully applied the model to describe the impact behavior of AD85 under uniaxial stress and one-dimensional strain conditions. This three-dimensional, continuum damage model [11] has been incorporated into the EPIC-2 finite element code [17]. Model constants were determined for the AD85 ceramic using static, SHB, plate impact, and bar-on-bar impact test data. This report describes the application of the Rajendran-Grove ceramic model to a problem in which a steel projectile impacts a layered ceramic target. The main objectives are: (1) to establish generality of the model constants, and (2) to demonstrate the model's ability to predict the measured stress history under multiaxial loading conditions. The center portion of the target in a ballistic test initially experiences one-dimensional strain, and later multiaxial strains due to the release waves. Only the shock and incipient damage phases of the penetration process are modeled. Vincent and Chang [18] performed a ballistic experiment in which a steel projectile impacted a layered AD85 (aluminum oxide) target. In the experiment, the shock stresses were measured using embedded manganin stress gauges at two locations inside the target. The measured stress history is influenced by the various shock/release waves: elastic-plastic compressive shock waves, release waves from the edges of the projectile-target, and fracture waves due to ceramic fracturing. Therefore, the modeling of a ballistic experiment under such complex wave interactions is indeed useful in the ceramic model validation. In the "Rajendran-Grove Ceramic Model" section, the salient features of the ceramic model are briefly described. The model parameters determination scheme for AD85 ceramic is also outlined. The "Modeling the Ballistic Impact Pressure Measurements" section briefly describes the ballistic experiment and discusses the various features of the ceramic model in reproducing the experimentally measured stress history. The "Summary and Conclusions" section follows the above sections. The damaged moduli expressions of Margolin [15] are provided in Appendix A.

### **Rajendran-Grove Ceramic Model**

Conventionally, the impact behavior of a material is described through a strength model and an equation-of-state (EOS). The strength model describes the variation of strength with respect to the strain rate, temperature, and pressure. The strength is expressed through the von Mises stress  $\sqrt{3}J_2$ , where  $J_2$  is the second invariant of the stress deviators. Therefore, the strength model involves the calculation of the deviatoric part ( $S_{ij}$ ) of the stress tensor  $\sigma_{ij}$ . The bulk (volumetric) behavior of the material is described by the EOS. This involves the calculation of the pressure (mean stress) part of the stress tensor.



## Constitutive Relationships

The total strain is decomposed into elastic and plastic strains as

$$\epsilon_{ij} = \epsilon_{ij}^e + \epsilon_{ij}^p \quad (1)$$

where the elastic strain consists of the elastic strain of the intact matrix material ( $\epsilon_{ij}^m$ ), and the strain due to crack opening/sliding ( $\epsilon_{ij}^c$ ),

$$\epsilon_{ij}^e = \epsilon_{ij}^m + \epsilon_{ij}^c \quad (2)$$

Since the strain components due to microcracking are elastic ( $\epsilon_{ij}^c$ ), represents both crack opening and closing. The matrix elastic strain and the microcracking strains are both proportional to the applied stress field. The plastic strains are calculated from viscoplastic flow equations. In the Rajendran-Grove ceramic model, Johnson and Cook [4] type strength model is employed to describe the strain rate dependent strength behavior. When voids (pores) are present in the ceramic, the strain components due to pore collapse are calculated from Gurson's pressure-dependent plastic flow equations [16]. The elastic strains in the microcracked void-free aggregate material are related to the stress tensor as follows:

$$\epsilon_{ij}^e = C_{ijkl} \sigma_{kl} \quad (3)$$

where  $C_{ijkl}$  are the effective compliance tensor components of the microcracked material. If  $C_{ijkl}$  is analytically inverted to the stiffness tensor components  $M_{ijkl}$ , the resulting stress state is

$$\sigma_{ij} = M_{ijkl} \left( \epsilon_{kl}^e \right) \quad (4)$$

The elements of the stiffness matrix  $C_{ijkl}$ , derived by Margolin [15,19] and Budiansky and O'Connell [20], are described in Appendix A. The total stress is decomposed into deviatoric stress and pressure components:

$$\sigma_{ij} = S_{ij} + P\delta_{ij} \quad (5)$$

The elastic stress-strain relationship between the deviatoric stresses and the corresponding deviatoric strains is given by

$$S_{ij} = 2G \left( \epsilon_{ij} - \epsilon_{ij}^p \right) \quad (6)$$

where  $e_{ij}$  are the total deviatoric strains,  $e_{ij}^p$  are the deviatoric plastic strains, and  $G$  is the degraded shear modulus due to microcracking and pores. When there are no pores,  $G$  will correspond to  $\bar{G}$  (see Appendix A) which is the shear modulus of microcracked ceramics. Therefore, the effective shear modulus (including the effects of both microcracks and pores)  $G (= R_g \bar{G})$  is calculated using the modified Mackenzie's relationship [21,22]:

$$R_g = (1 - f) \left( 1 - \frac{(6\bar{K} + 12\bar{G})f}{(9\bar{K} + 8\bar{G})} \right) \quad (7)$$

$R_g$  is the shear modulus correction factor for spherical pore content in the ceramic.  $f$  is the porosity content (void volume fraction), and  $\bar{K}$  is the microcracks-degraded bulk modulus. The equation of state is described by the following modified Mie-Gruneisen relationship.

$$P = R_k \left[ \bar{P}_{11} (1 - 0.5 \Gamma \mu) + \Gamma \rho_0 (1 - l_0) \right] \quad (8)$$

where

$$\bar{P}_{11} = (\bar{K} K) (\beta_1 \mu + \beta_2 \mu^2 + \beta_3 \mu^3) \quad (9)$$

$\mu (= 1 - \frac{V}{V_0})$  is the elastic volume compressibility (strain) and  $\beta_1$ ,  $\beta_2$ , and  $\beta_3$  are the empirical parameters.  $\Gamma$  is the Mie-Gruneisen parameter,  $\rho_0$  is the material's initial density,  $l_0$  is the initial value of internal energy, and  $l$  is the current internal energy. The Mackenzie's correction factor  $R_k$  is given by

$$R_k = \frac{(1 - f)}{\left( 1 + \frac{3\bar{K}f}{4\bar{G}} \right)} \quad (10)$$

where,  $R_k \bar{K}$  is the degraded bulk modulus due to pores and microcracks. In the absence of voids and microcracks, Equation 8 reduces to the Mie-Gruneisen EOS for the undamaged, flawless material.

### Definition of Damage

In the ceramic model, microcrack damage is measured in terms of a dimensionless microcrack density  $\gamma$ , where

$$\gamma = N_0^* a_{\max}^3 \quad (11)$$

$N_0^*$  is the average number of microflaws per unit volume in the ceramic which is a model constant.  $a_{\max}$  is the maximum microcrack size which is treated as an internal state variable. Microcrack extends when the stress state satisfies the Griffith criterion [23]. As the microcracks extend,  $\gamma$  increases and the stresses relax. In the model  $N_0^*$  is assumed to be constant. Therefore, the increase in  $\gamma$  is due to increase in the crack size. In the "Rajendran-Grove Ceramic Model" and "Modeling the Ballistic Impact Pressure Measurement" sections, the microcrack growth law is defined using a dynamic fracture mechanics based relationship.

In general, the phases of damage evolution consists of: (1) nucleation of microcracks with some initial crack density, (2) growth of microcracks, and (3) coalescence of the microcracks at some critical crack size. At present, no means exist to experimentally measure and quantify the variation of crack size, crack density, and number of cracks with respect to time. However, the effects of microcracks evolution can be introduced into the constitutive equations through appropriate physically based laws/equations.

#### Microcrack Nucleation

One simplified approach is the following: The microcracks are assumed to exist prior to any loading; therefore, the initial crack density  $\gamma_0$  is determined from the relationship (see Equation 11) using the values for the two material constants:  $N_0^*$  and  $a_{\max}$ .

The microdamage (microcrack size) will not increase until the generalized Griffith criterion (Margolin [24] and Dienes [25]) is satisfied either under shear loading or under tensile loading. Note that the shear loading could occur under both tensile and compressive pressures. The microdamage rate is zero until the applied strain energy release rate  $G_I$  exceeds a critical value  $G_c$ . The strain energy release rate (note that the rate refers to crack extension, not the "time") under mode I crack opening for a general loading ( $\sigma_{ij} \neq 0$ ) is given by:

$$G_I^+ = \frac{4(1-\nu^2)}{\pi E} a_{\max} \left[ \sigma_{kk}^2 + \frac{2(\sigma_{ik}^2 + \sigma_{jk}^2)}{2-\nu} \right], i \neq j \neq k \quad (12)$$

where  $\sigma_{kk}$  are the normal stresses,  $\sigma_{ik}$  and  $\sigma_{jk}$  are the shear stresses,  $a_{\max}$  is the size of the largest microcrack, and  $\nu$  and  $E$  are undamaged Poisson's ratio and Young's modulus, respectively. The repeated index 'k' does not mean summation. When the crack surfaces are perpendicular to tensile principal stresses  $\sigma_I$ , then Equation 12 is evaluated with  $\sigma_{kk} = \sigma_I$  and  $\sigma_{jk} = \sigma_{ik} = 0$ . Under general loading conditions ( $\sigma_{ij} \neq 0$ ), the strain energy release rate for mode II and mode III is expressed as

$$G_I^- = \frac{8(1-\nu^2)}{\pi E(2-\nu)} a_{\max} \left[ \sqrt{\bar{\sigma}_{ik}^2 + \bar{\sigma}_{jk}^2} - \tau_0 + \mu \bar{\sigma}_{kk} \right]^2, i \neq j \neq k \quad (13)$$

where  $\tau_0$  is the cohesion stress and  $\mu$  is the friction coefficient. In this case, only modes II and III are active and the normal stresses serve only to resist the shearing stresses. Defining  $G_{\max}$  to be the maximum of all values of  $G_I^+$  and  $G_I^-$ , microcracks are assumed to have extended if  $G_{\max}$  exceeds the critical crack energy release rate  $G_c$ , where

$$G_c = 2T \quad (14)$$

and

$$T = \frac{K_{\text{eff}}^2 (1-\nu^2)}{2E} \quad (15)$$

Equation 15 defines the surface tension  $T$  as a function of effective critical fracture toughness ( $K_{\text{eff}}$ ), Poisson's ration ( $\nu$ ), and Young's modulus ( $E$ ) in the undamaged material. In the model application, the critical effective stress intensity factor is assumed to be equal to simply the static fracture toughness ( $K_{IC}$ ) under crack opening mode. At present, the fracture toughness is treated as a material constant which will not vary with strain rate. John [26] experimentally determined the strain rate dependent fracture toughness values for brittle concrete. Though such a study does not exist for ceramic materials, especially at high strain rates, it is still possible to include strain rate effects on the fracture toughness in the model formulation based on his study.

### Damage Growth Model

The damage evolution equation is derived from the fracture mechanics based relationship [27] for a single crack propagation under dynamic loading conditions. An evolution law for the state variable  $a_{\max}$  is described through a strain energy release based microcrack growth rate law of the form

$$\dot{a}_{\max} = n_1 C_R \left[ 1 - \left( \frac{G_c}{G_{\max}} \right)^{n_2} \right] \quad (16)$$

where  $C_R$  is the Rayleigh wave speed,  $G_c$  is the critical strain energy release for microcrack growth, and  $G_I$  is the applied strain energy release. The model constants  $n_1$  and  $n_2$  can be used to limit the microcrack growth rate.  $n_1$  and  $n_2$  are damage growth constants. Since the crack growth based damage rates are different under tensile and compressive loadings, these constants will be assigned different values.

When the crack density reaches a critical value of 0.75 (see Reference 11), the model assumes that the microcracks have coalesced, leading to pulverization of the ceramic. Henceforth, the material has no strength in tension and its compressive strength follows a Mohr-Coulomb law, as in

$$Y = \begin{cases} 0, & P \leq 0 \\ \alpha_p + \beta_p P, & P > 0 \end{cases} \text{ when } Y = 0.75, \quad (17)$$

where  $Y$  is strength,  $P$  is pressure, and  $\alpha_p$  and  $\beta_p$  are model constants for the pulverized material. The pressure is computed from:

$$P = \begin{cases} 0, & \epsilon_v^e \geq 0 \\ -\bar{K}_p \epsilon_v^e, & \epsilon_v^e < 0 \end{cases}, \quad (18)$$

where  $\epsilon_v^e$  is engineering elastic volumetric strain (see Equation 2) and  $\bar{K}_p$  is the bulk modulus for pulverized material. With this approach, each pulverized element in a finite element mesh may have its own distinct values of  $\bar{K}_p$  and  $\bar{G}_p$ . It is also possible to input new values for  $K$  and  $G$  as bulk and shear moduli of the pulverized ceramic; this will increase the number of model constants by two.

#### Model Parameters Determination

The static compressive strength of AD85 ceramic has been measured at about 2 GPa. The SHB test data (strain rate  $\approx 10^3$  s) indicate that its unconfined dynamic compressive strength is about 3 GPa [11]. From plate impact test measurements, the dynamic compressive strength of AD85 at extremely high strain rates ( $\approx 10^5$  s) is about 5.5 GPa. This strength increase is due to a combined strain rate and confined pressure effect. While the confining pressure effect was implicitly modeled by the stress-strain relationship (see Equation 4), the compressive strength variation with respect to strain rate is described by (Johnson and Cook model with  $C_2 = 0$ ):

$$Y = C_1 (1 + C_3 \ln \dot{\epsilon}) \quad (19)$$

The constants  $C_1$  and  $C_3$  are calibrated using the strength values obtained from the plate impact and SHB tests. The corresponding values are:  $C_1 = 4.0$  GPa and  $C_3 = 0.03$  GPa. When the strain rates are low ( $< 1000$ /sec) and the stress state is uniaxial, the ceramic strength is controlled by the microcracking feature of the model; therefore, the SHB data are reproduced by adjusting the microcrack model constants, especially the frictional coefficient  $\mu$ . The model assumes plastic flows in ceramics when the shock pressures are above the Hugoniot elastic limit. The total strain includes elastic, cracking, and plastic components. The plastic strains are calculated using conventional plastic flow theories.

There are six constants in the Rajendran-Grove ceramic model to describe the microcracking behavior:  $K_{IC}$ ,  $\mu$ ,  $N_0^*$ ,  $a_0$ ,  $n_1$ , and  $n_2$ . Note that the cohesion stress  $\tau_0$  in Equation 13 is assumed to be zero and, therefore, this constant is not considered in the present study. The preliminary set of the model constants is determined from SHB and plate impact experimental data.

To assure generality of the model constants, manganin gauge measured stress data from the bar-on-bar impact experimental configuration was also considered. The best suitable values for the constants are obtained based on the ability to reproduce the experimental data from SHB, plate impact, and bar-on-bar impact configurations. Rajendran [11] and Rajendran and Grove [14] reported this model determination scheme and determined the model constants for AD85 ceramic. The corresponding constants are given in Table 1.

Table 1. Model constants for AD85 ceramic

Symbol	Value	Description
$K_{IC}$	3 MPa $\sqrt{m}$	Static fracture toughness
$\mu$	0.72	Coefficient of friction
$N_0^*$	$1.83 \times 10^{10} m^{-3}$	Microcrack density (numbers/volume)
$a_0$	$58 \times 10^{-6} m$	Initial microcrack size
$n_2$	0.07	Crack growth rate power index
$n_1^+$	1.0	Tensile crack growth rate index
$n_1^-$	0.1	Compressive crack growth rate index

The value for  $K_{IC}$  is obtained from fracture mechanics handbooks. With lack of any microscopic measurements a large value for the number of flaws in the ceramics,  $N_0^*$  has been arbitrarily assumed. It may also be assumed that the number of flaws is proportional to the number of grains per unit volume and attempt to estimate this constant. However, in the present work no such attempt was made.

The plate impact simulations revealed that the initial maximum crack size  $a_0$  and the crack growth indices  $n_1$  and  $n_2$  controlled the shape of the unloading portion of the stress-time history profile of the plate impact data. The arrival of a very weak spall signal at point B in Figure 1 is found to be sensitive to the crack size. In the simulation, the shape between points B and C was influenced by the growth constants. Therefore, the initial estimates for these two damage growth constants,  $n_1$  and  $n_2$ , were calibrated to reproduce the stress profile measurements in a bar (uniaxial stress state) and in a plate (one-dimensional strain state).

In metals, the experimentally measured crack propagation speed under mode I (crack opening) is equal to the fraction of the Rayleigh wave speed [27]. However,  $n_1^+$  is set to one for AD85 ceramic. The crack propagation speed under shear (mode II or mode III) is relatively lower than under mode I and, therefore, a value of 0.1 is assumed arbitrarily for  $n_1^-$ . For  $n_2$ , a value of 0.07 was determined based on the model's ability to reproduce the rod-on-rod experimental data (see Figure 2).

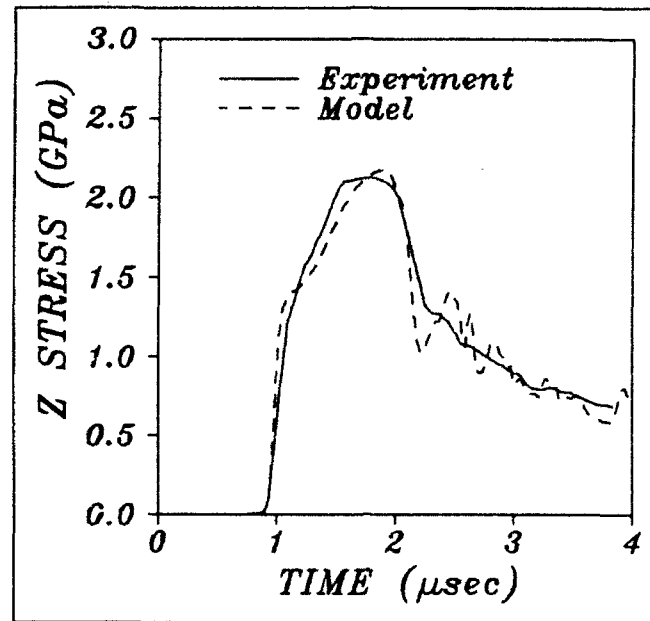


Figure 1. A comparison between model and measured stress history in a plate impact experiment on AD85 target.

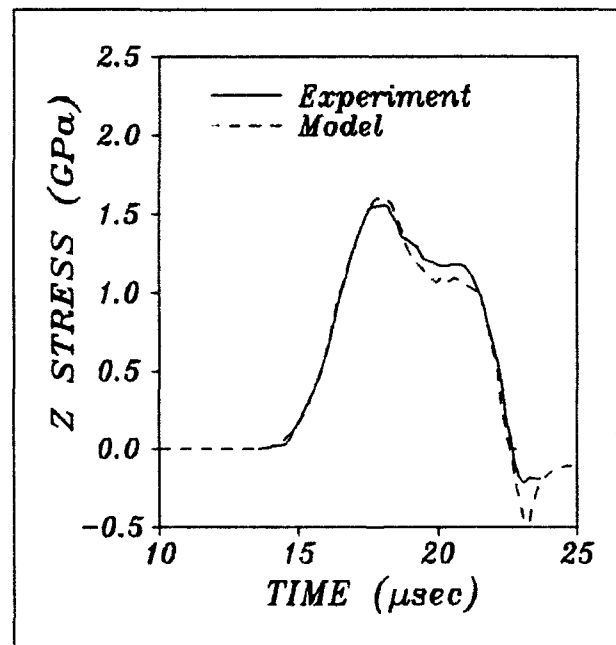


Figure 2. A comparison between model and measured stress history in an AD85 bar-on-bar experiment.

The model parameters estimation scheme requires a trial and error basis of adjusting the crack growth indices between different experimental configurations. Unfortunately, there is no one set of unique values for the impact damage model parameters. This is true for all the ceramic models in References 3, 5, 8, 9, and 11. At best, a suitable set of values can be successfully determined through a trial and error basis of reproducing a variety of experimental configurations. The model constant evaluation procedure is given by Rajendran and Grove [14].

While Figure 1 compares the model generated stress history using the constants from Table 1 with the one-dimensional strain data from the plate impact test, Figure 2 compares the model prediction with uniaxial stress data from the bar-on-bar impact test.

### Modeling The Ballistic Impact Pressure Measurements

Vincent and Chang [18] conducted instrumented ballistic experiments on ceramic targets. A schematic of the target configuration is shown in Figure 3. Two manganin gauges were embedded into the target assembly: the first (top) gauge is placed between the front ceramic and the isodamp, and the second (bottom) gauge is placed between the back face of the isodamp and the second ceramic. This second ceramic is backed by a thick aluminum plate.

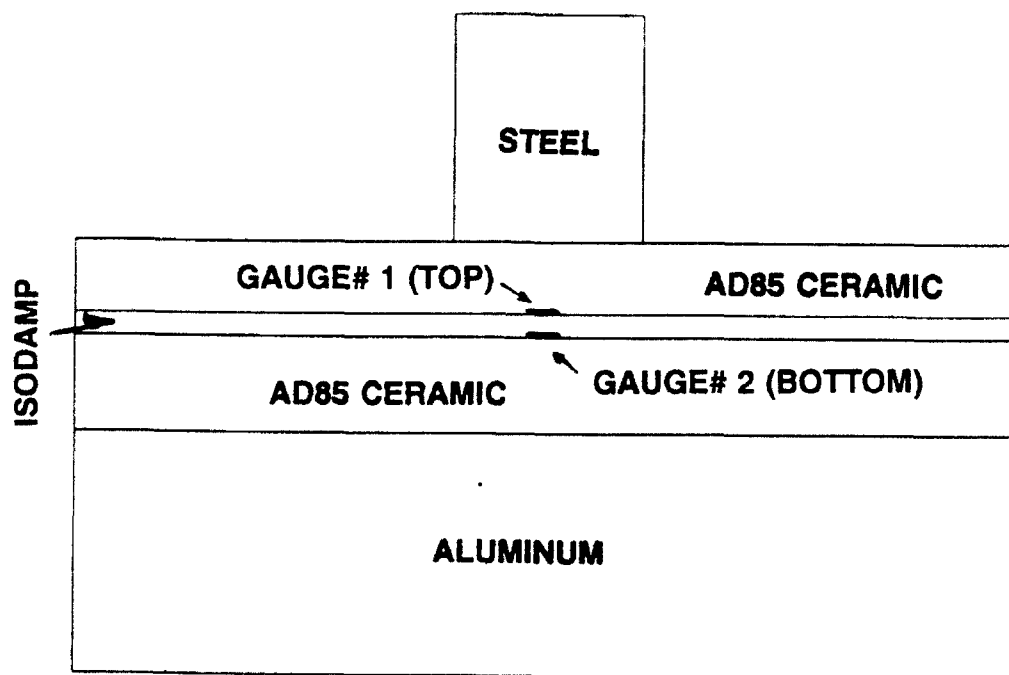


Figure 3. A schematic of the instrumented ballistic experiment.



The top gauge measurements seemed to be valid only for a very short time ( $<2$  microseconds). The ceramic material that surrounds this top gauge is destroyed by the cracked ceramic. However, the bottom gauge survived during the measuring period (about 8 microseconds to 10 microseconds). This gauge is protected by the intact second ceramic and isodamp. However, the bottom gauge is also eventually destroyed. Unfortunately, from these destructive tests it is not possible to determine the timings of events such as the onset of microcracking or growth of macrocracks, therefore, the different events which might occur inside the target during the projectile penetration can only be indirectly related to the various features of the stress gauge signal. The data from the two gauges are shown in Figure 4. The pulse duration and amplitudes are sensitive to the shock response of the ceramics, isodamp, and projectile.

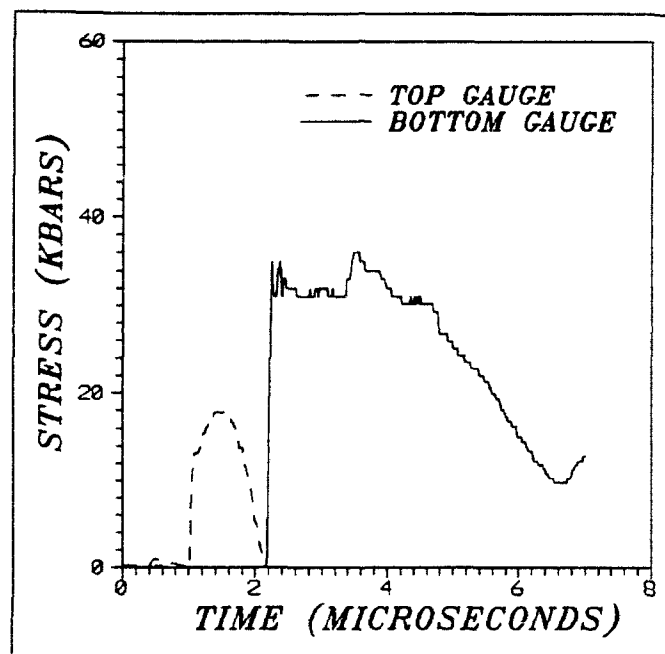


Figure 4. Manganin gauge measured stress histories in a ballistic experiment.

### The Ballistic Experiment

The ballistic experiment of Vincent and Chang [18] was modeled using the 86 version of the EPIC-2 code. Table 2 provides the details of simulation and experiment. There are six layers of materials in the target assembly: (1) ceramic (AD85), (2) top gauge package, (3) isodamp, (4) bottom gauge package, (5) ceramic (AD94), and (6) aluminum. The gauge records the stress-time history experienced by the isodamp. The target dimensions in the simulation are given in Table 3. In the simulation, the top and bottom ceramics are modeled as AD85.

Table 2. Projectile dimensions and materials

Details	Experiment	Modeling
Length (mm)	29.464	30.0
Diameter (mm)	19.989	20.0
Material	Steel	Steel
Velocity	793.0	790.0

Table 3. Target dimensions

Layers	Thickness (mm)
AD85 ceramic	9.525
Isodamp	3.0
AD85 ceramic	12.7
5083 aluminum	31.75

### Simulation Details

The steel and aluminum were respectively modeled using the HY100 steel and 2024-T351 aluminum models in the 86 version of EPIC-2 library. Since the aluminum is expected to remain mostly elastic in the present calculations due to attenuation of the wave amplitude, the stress histories at the gauge locations should not be influenced by the plastic behavior of aluminum. In fact, simulations with different aluminums produced almost identical stress histories. The Johnson and Cook strength model described the strain rate dependent strength of these materials. The Mie-Gruneisen EOS was employed to describe the bulk (pressure-volume) behaviors.

The isodamp was modeled as an elastic-perfectly plastic solid with a dynamic yield strength of 0.4 GPa [28]. The ceramic strength model constants (see Equation 19) are  $C_1 = 4$  GPa and  $C_3 = 0.03$ . The EOS is described by the Mie-Gruneisen relationship (see Equations 8 and 9). The material density, shear modulus, and EOS constants for isodamp and AD85 ceramics are given in Table 4.

Table 4. Material constants for isodamp and AD85 ceramic

Material constants	AD85 ceramic	Isodamp
Density (gm/cm <sup>3</sup> )	3.42	1.29
Shear modulus (GPa)	108	0.5
$\beta_1$ (GPa)	188	3.9
$\beta_2$ (GPa)	188	16.3
$\beta_3$ (GPa)	0	42.0
$\Gamma$	1.0	0.738

### Results and Analyses

To understand the effects of various deformation processes in the ceramic material on the calculated stress histories (at the gauge locations), a number of simulations of the ballistic experiment were performed. For this purpose, the following cases were considered:

- Elastic (Case E)
- Elastic-Plastic (Case EP)
- Elastic-Cracking (Case EC)
- Elastic-Plastic-Cracking (Case EPC)

These various cases were simulated by properly adjusting the model parameters. For instance, the cracking is eliminated by setting the initial crack size  $a_0$  to zero. The plastic flow is eliminated by setting the strength model constant  $C_1$  to a large number. To suppress plastic pore collapse, the void content  $f_0$  is set to zero. In the present analysis, the ramping of the plastic wave in the plate impact test data is assumed to be due to both strain rate and pore collapsing in AD85. The bulk of the analyses of the EPIC-2 generated results is based on the stress history comparisons between the experiment and each of these cases. The effects of time step and mesh on the stress history were also investigated.

### Grid and Time Step

The EPIC-2 simulation of the ballistic experiment idealizes the projective target configuration as an axisymmetric geometry, as shown in Figure 5. As shown in the experiment, the radii of the target layers in the simulations were sufficiently large (five times the projectile radius) to prevent stress reflections from the lateral boundaries influencing the calculated stress histories. The minimum grid size for the entire mesh was selected based on the number of rows of elements and the element size in the isodamp. To ensure realistic and accurate results, the isodamp was modeled using four rows (layers) of elements; therefore, for an isodamp layer of 3 mm thickness, the element thickness was 0.75 mm. This element size was the standard for determining the number of rows of elements in the projectile, as well as in the other target layers.

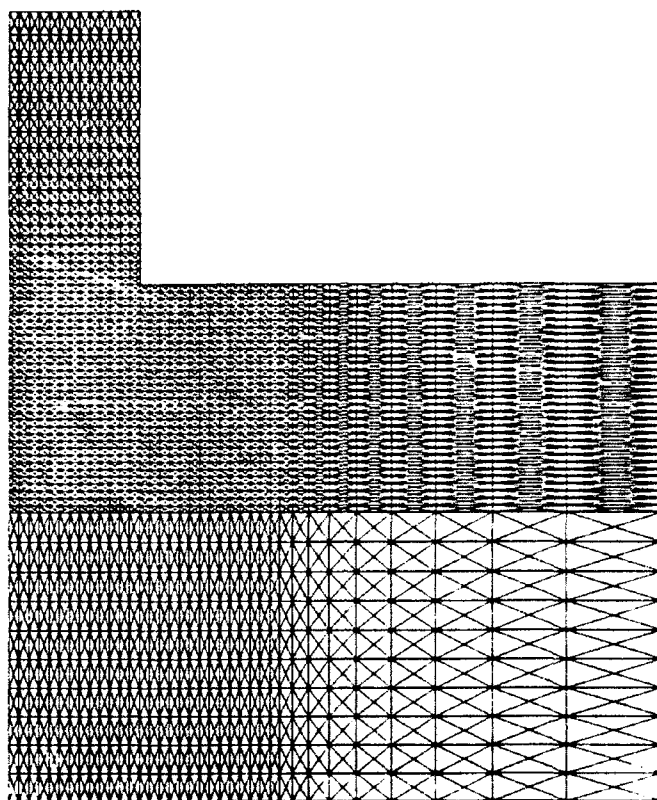


Figure 5. The finite element mesh for the ballistic experiment.

The total number of nodes in the projectile was 554 and the target was 3888. The number of elements in the projectile was 1040 and the target was 6048. The element aspect ratio was kept closer to one in the vicinity of the impact planes and gauge locations, as can be seen from the finite element grid shown in Figure 6. In general, the numerical results from the shock wave based finite element/difference codes (called the hydrocodes) are inherently sensitive to element aspect ratio and the mesh type; therefore, it is important to design suitable grids for realistic and accurate results from the code calculations. For this reason, several meshes were considered and the repeatability of results was verified. While keeping the mesh reasonably fine, a variation in the element aspect ratio was introduced between two different meshes. The mesh with an aspect ratio of one for the isodamp and two for the ceramic compared very well with the standard mesh with an aspect ratio of one for both isodamp and ceramics.

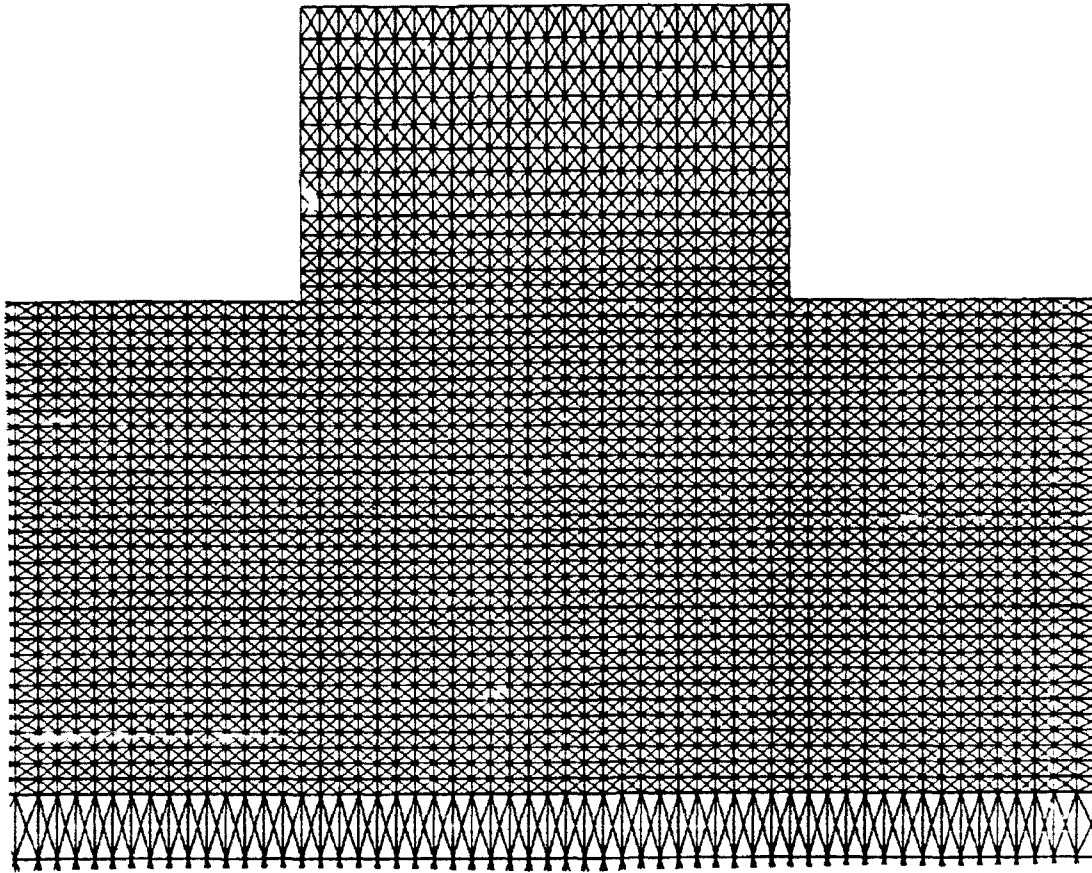


Figure 6. A close-up view of the finite element mesh near the impact region.

Figure 7 shows that the calculated stress histories at the bottom gauge location are compared for two different meshes. A slight mesh effect on the stress histories can be seen from the plot. However, the overall shape and stress levels for the two meshes were practically the same. The element size for the ceramic in the coarse mesh was twice the element size for the isodamp. Interestingly, the coarse mesh with an aspect ratio of 2 for the ceramic produced smoother stress history than the fine mesh.

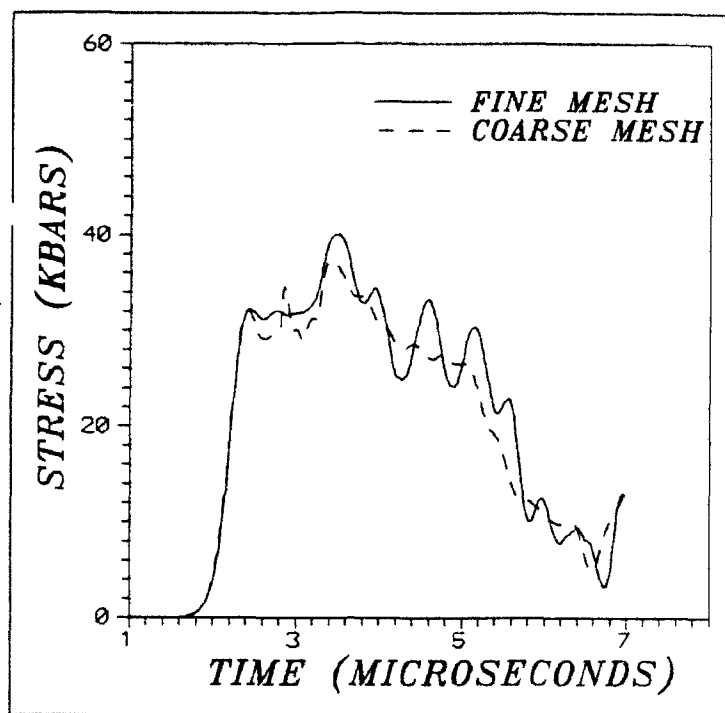


Figure 7. Effects of mesh on stress history

In the EPIC code, one of the parameters that controls the time step size is the "ssf" parameter. The time step can be controlled by setting values between 0.1 and 0.9 for ssf. It is also possible to examine the time step effects through a parameter which controls the maximum allowable time step. The results for the  $ssf = 0.1$  (small time step) and 0.9 (large time step) are compared in Figure 8. The stress time histories are similar except for some minor stress oscillations. These results provide sufficient confidence in the numerical results. One of several other code parameters, such as the maximum allowable time step, can also influence the numerical results; however, the proper choice of these time step related code parameters produce similar and repeatable results.

#### Elastic (Case E)

The simplest stress-strain relationship is the Hooke's Law for an elastic material. Since ceramic is a brittle solid, it is proper to begin the analysis with an elastic description. The inelastic strains due to both microcracking and plastic flows are not allowed in the elastic simulation. The shear and bulk moduli will not degrade and will remain intact under impact loading. The strength of the ceramic is unlimited; therefore, failure is not allowed in the elastic case. The results from this case is presented in Figures 9 and 10. The bottom stress gauge data are compared with the simulation in Figure 9. As can be seen from this figure, the calculated stress levels are higher and the loading duration is lower when compared to the data. These results clearly indicate that a simple elastic assumption is inadequate for describing the complex impact behavior of ceramic materials.

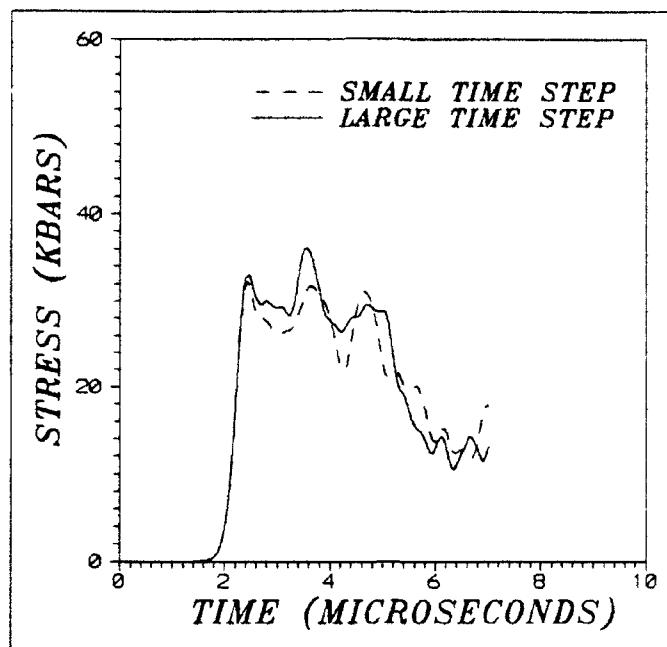


Figure 8. Effects of time step on stress history.

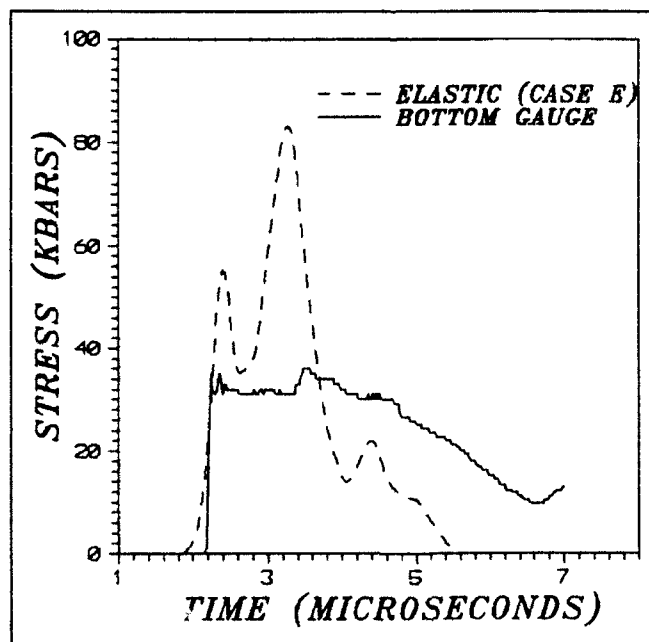


Figure 9. A comparison between bottom gauge data and Case E. The ceramic behavior is assumed elastic.

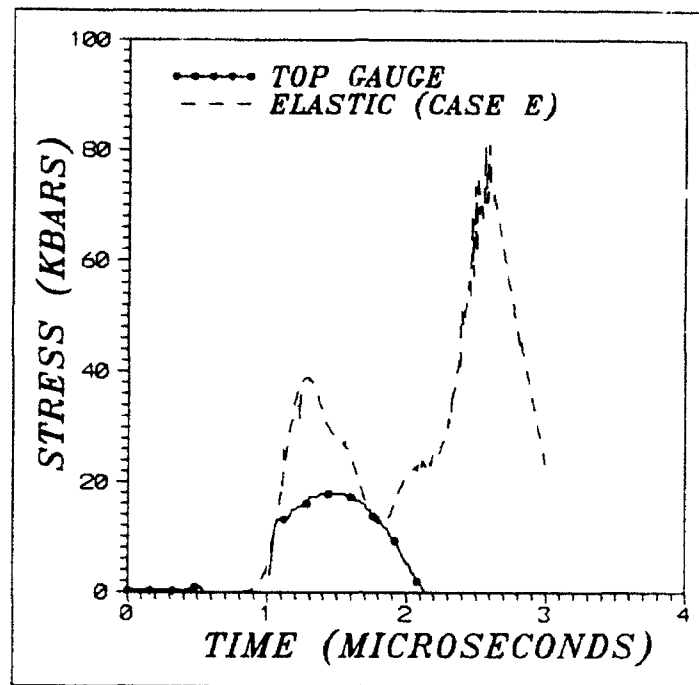


Figure 10. A comparison between top gauge data and Case E. The ceramic behavior is assumed elastic.

A comparison between the top gauge and the elastic simulation, as shown in Figure 10, further confirms the inadequacy of simple elastic description of the ceramic. However, the top gauge record is questionable beyond 2 microseconds. In the experiment, the fractured ceramic that surrounds the gauge destroyed the gauge beyond this time. This was confirmed by Vincent and Chang [18] through several experiments. The gauge measurements did not show the arrival of a second strong shock as it did in the simulation; the simulation clearly showed the arrival of a strong second shock. A relatively simple wave analysis under one-dimensional strain condition (as in the plate impact experiment) shows that the second shock arrives from the boundary between the isodamp and the bottom ceramic due to an overwhelming impedance mismatch between the two layers.

The absence of such second shock in the test imply that the top gauge data may be reliable only for the first 2 microseconds. A carbon gauge (placed in addition to a manganin gauge) showed the arrival of a second shock; however, this gauge was also destroyed within 3 microseconds after the impact. It is also possible that the apparent second shock in the carbon gauge signal could be an artifact of gauge failure. Since only one experiment was conducted with the carbon gauge, a definite conclusion could not be made. The measured maximum stress amplitude in the top gauge seems to be a reliable data. An approximate one-dimensional strain analysis based on the impact shock amplitude in the ceramic and the impedance match solution between the isodamp and ceramic seems to support this conclusion.



### Elastic-Plastic (Case EP)

In the elastic-plastic simulation, the impact behavior of ceramic was described through the strain rate dependent strength in Equation 19. An initial value of zero for the microcrack size eliminates microcracking in the calculation. The initial porosity was also set to zero so that pore collapse would not occur. Since the shock waves in the ballistic experiment are spherical, it is not possible to accurately determine the different wave arrival times. However, the rough estimates of shock arrival times based on the one-dimensional strain analysis sometimes provide guidelines for interpreting the gauge signal. In Figure 11, the elastic wave arrives at the gauge location at about 2 microseconds. A weaker release wave from the edge of the projectile follows this initial elastic wave and unloads at point A. A reshock (compressive loading) later arrives from the interface of the isodamp and bottom ceramic at point B. The unloading waves from the free surfaces of the top ceramic unload the stresses at point C. In the experimental data, the sharp peak at point A, as well as the strong second shock, are not found.

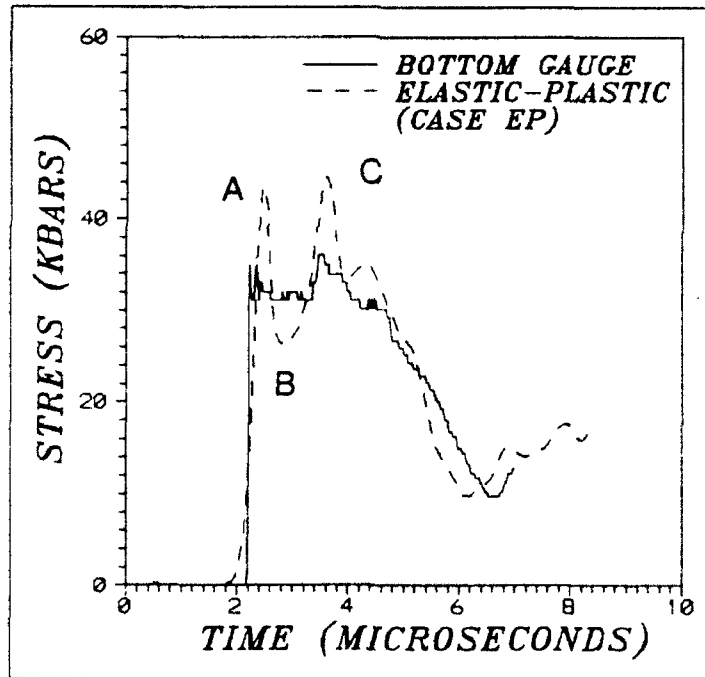


Figure 11. A comparison between bottom gauge data and Case EP. The ceramic behavior is assumed elastic-plastic (no cracking).

When the ceramic behavior is described by an elastic-plastic model, the model comparison with the bottom gauge data improved significantly, as shown in Figure 11. It appears that limiting the ceramic compressive strength to finite values through a yield surface could improve the model prediction. With lack of any microstructural evidence to prove macroplastic flows in the brittle ceramic under impact loading conditions, it is premature to conclude that AD85 ceramic deforms plastically like a metal.

just because the elastic-plastic model reproduced the experimental measurements. There is also a possibility to cap, or limit, the ceramic strength due to microcracking and crushing. Though the matching is good, the absence of certain salient features in the simulation indicates elastic-plastic idealization alone may not be reproducing all the features. It appears that the matching between the simulation and experiment can be significantly improved by limiting the ceramic strength to finite values (see Equation 19). To further verify the results from the elastic-plastic idealization, a comparison between simulation and top stress gauge data is made in Figure 12. The arrival of the second shock at point B can be clearly seen in the simulated stress history.

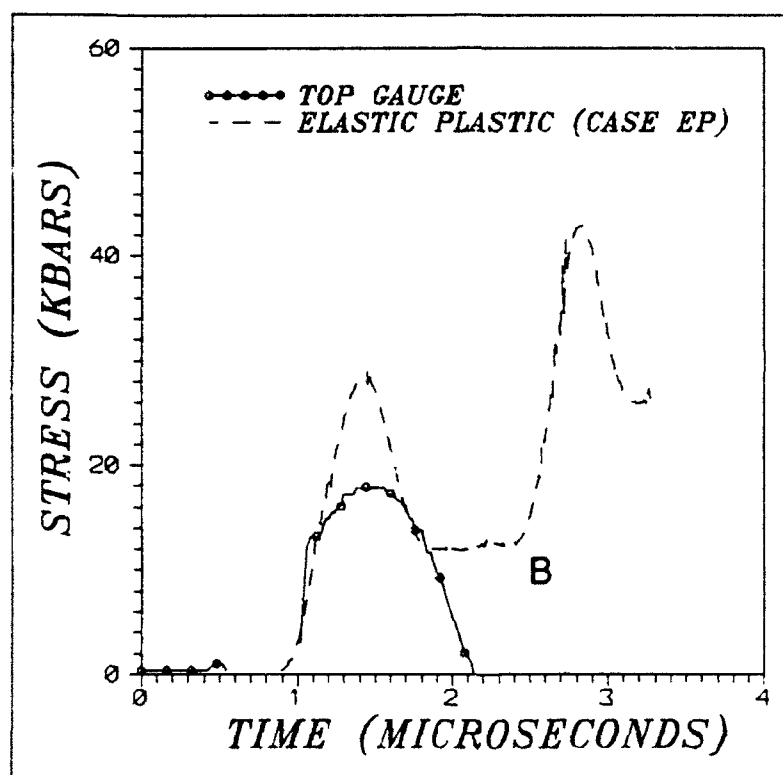


Figure 12. A comparison between top gauge data and Case EP. The ceramic behavior is assumed elastic-plastic (no cracking)

#### Elastic-Cracking (Case EC)

This case examines the effect of microcracking on the stress profile. In the simulation, a large value for the constant  $C_1$  in Equation 19 was assumed to eliminate plastic flows. The strength was degraded or relaxed through microcracking only. The viscoplastic pore collapsing was also suppressed in the simulation. Figure 13 compares the calculated stress history from the elastic-cracking case and the bottom gauge data. The two stress peaks (at points A and C) were present as in Cases E and EP.

The stress levels are instantaneously higher compared to the gauge data. The stress history during loading and unloading matched with the data somewhat in an average manner. Interestingly, the results from Case EP (elastic-plastic) compared relatively better with the data than this elastic-cracking case. These results further confirm that the ceramic behavior is much more complex than the assumptions of either elastic-cracking or elastic-plastic.

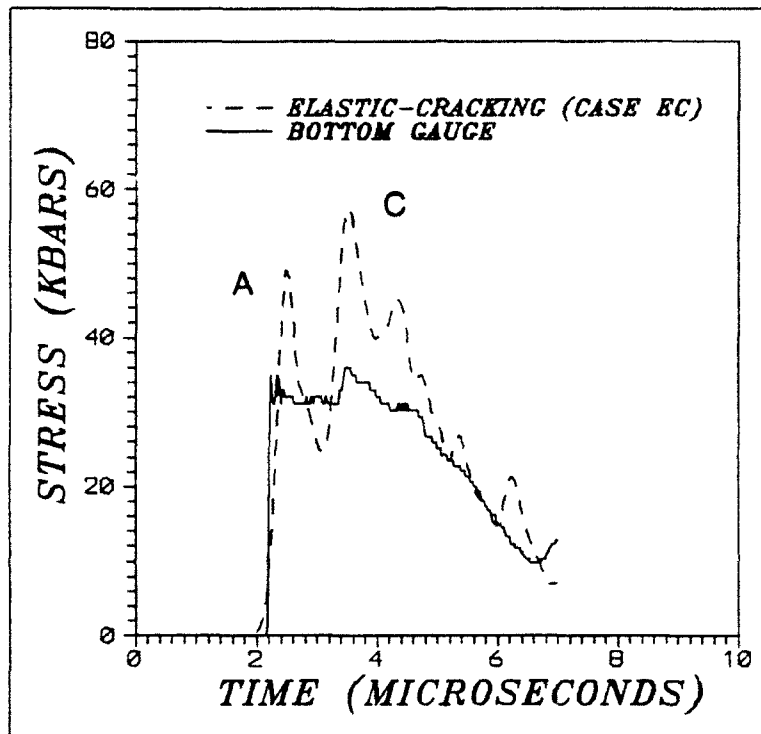


Figure 13. A comparison between bottom gauge data and Case EC. The ceramic behavior is assumed elastic cracking (no plastic flow).

#### The Full Ceramic Model (Case EPC)

To further investigate the effects of inelastic deformations on the stress history, the elastic-plastic cracking case with pore collapse was considered. In other words, the Rajendran-Grove ceramic model was used to describe the impact behavior of AD85 under Case EPC. The ballistic impact experiment of Vincent and Chang [18] was simulated using the ceramic model constants in Table 1. A 10% porosity content and an initial flaw size of 0.057 mm were used in the simulation. Figure 14 compares the model and the bottom gauge data.

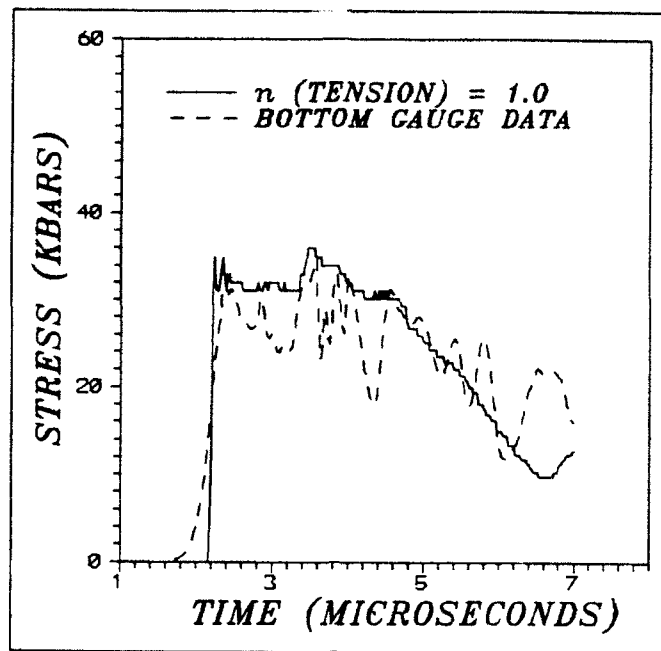


Figure 14. A comparison between the ceramic model (with tensile  $n_1 = 1$ ) and bottom gauge data.

The model showed a lower stress level and a higher pulse duration compared to the data. The analysis indicated an excessive tensile damage in the ceramic. Several regions of the top ceramic plate had fractured. Since the Rajendran-Grove ceramic model degrades the ceramic strength due to microcracking, the microcracks induced damage significantly lowering the stress amplitude.

To further investigate the ceramic model results, damage shade plots, as shown in Figures 15 and 16, were generated. The regions without any shade are free of damage. The damage evolution at 4 microseconds is shown in Figure 15. The maximum damage was about 0.14. This occurred at a location 2 mm in depth and a 13 mm radius (from the axis of symmetry) which corresponds to the Hertzian crack vicinity. The ceramic model could indicate the formation of classical Hertzian cracks emanating at about a  $45^\circ$  angle from the edge of the projectile-target interaction regions.

The damage shade plot at 8 microseconds is shown in Figure 16. The maximum damage occurred in regions closer to the top gauge location. Since the isodamp is a low impedance and low strength material, the impact loading conditions create large biaxial tensile stresses in the ceramic. Therefore, at the gauge location, tensile damage evolves rapidly and fractures the ceramic. Since ceramic is extremely weak in tension and strong under compressive loading, the tensile regions start fracturing first. When damage reaches a value of one, the ceramic is assumed to have failed completely, and the failed elements will not sustain any tensile loading. However, those elements continue to carry compressive loading until the material pulverizes under compression.

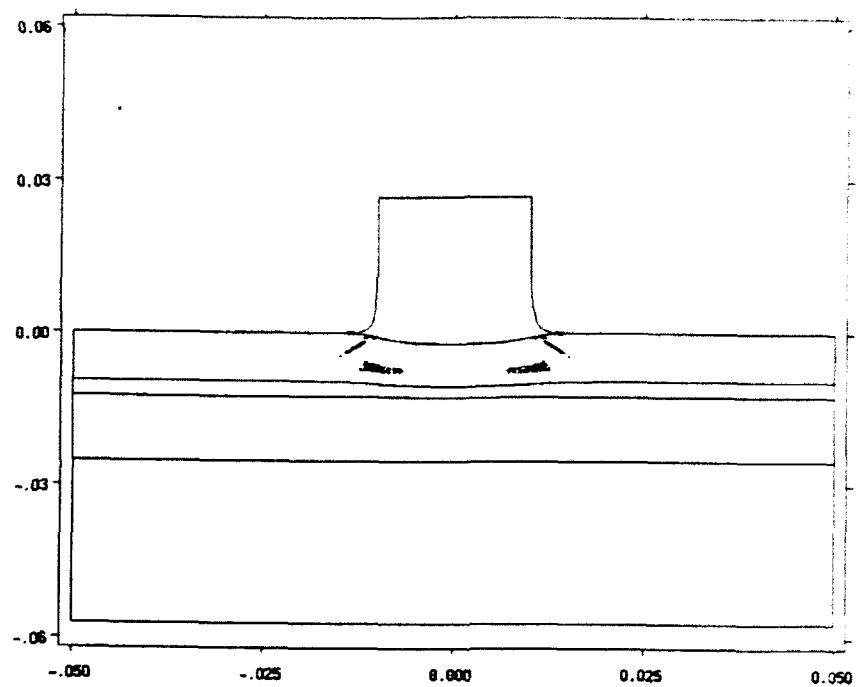


Figure 15. The microcracking damage shade plot at time 4 microseconds.

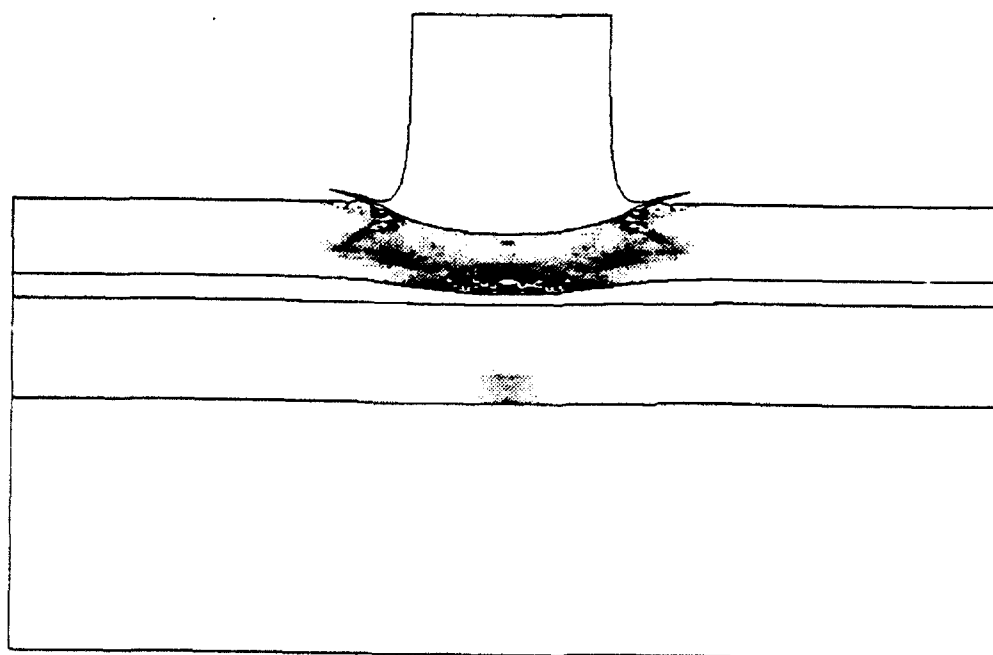


Figure 16. The microcracking damage shade plot at time 8 microseconds.

While the projectile penetrates into the top ceramic layer, damage due to microcracking develops in the bottom ceramic which is separated from the top ceramic layer by the isodamp. The plots of damage shade in the bottom ceramic layer corresponds to very low values ( $<0.05$ ) of the damage. The mild plastic flow near the axis-of-symmetry at the top surface of the aluminum causes tensile loading in ceramic. These tensile stresses initiate damage in the bottom ceramic, as shown in Figure 16.

In the analysis, a value of 1.0 for  $n_1^+$  overestimated the tensile damage in the top ceramic plate. According to the microcrack growth rate in Equation 16, the limiting crack growth rate is equal to the Rayleigh wave speed when  $n_1^+ = 1$ ; therefore, to improve the matching between the experiment and the model, the tensile crack growth index  $n_1^+$  is reduced from 1.0 to 0.1 and the ballistic experiment was simulated again. All the other constants in Table 1 were not modified. Recall that both the elastic and elastic-plastic simulations showed a strong second shock arriving at the top gauge location at about 2.4 microseconds. Though the data did not show any second shock, the maximum amplitude of the first shock recorded by the gauge was a reliable data. Therefore, to further verify the stress history at the top gauge location, a comparison between the model and the data is made in Figure 17. As can be seen from this figure, the elastic-plastic cracking simulation also showed the second shock at about 2.4 microseconds.

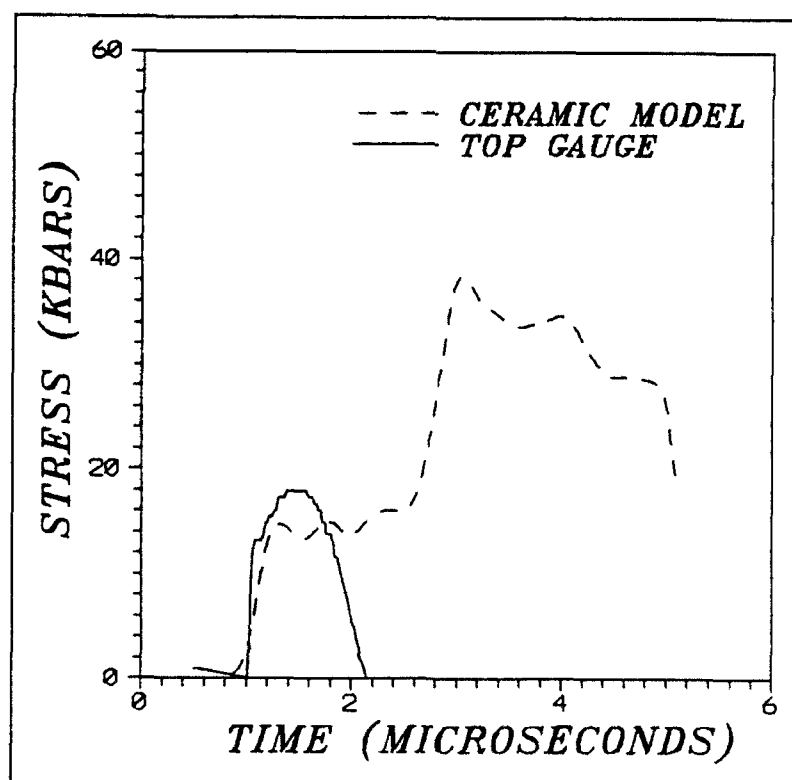


Figure 17. A comparison between top gauge data and the ceramic model (with tensile  $n_1 = 0.1$ ).

It is also worth recalling that the simulated peaks in the elastic and elastic-plastic cases were 40 Kbars and 30 Kbars (10 Kbars  $\approx$  1 GPa), respectively. These values are significantly higher compared to the measured maximum stress of 19 Kbars. However, the model calculated peak of about 17 Kbars compares well with the data.

To further analyze the ceramic model predictions, a comparison between the model generated stress history and measured stress history (bottom gauge) is shown in Figure 18. As can be seen from this figure, the model reproduced the experimental data extremely well. Both the amplitude and the pulse duration matched between the model and the data. The value of 0.1 for the tensile crack growth rate parameter improved the model prediction significantly. Since this parameter indirectly controls the amount of stress relaxation in the model, a reduced value for this parameter accordingly increased the calculated stress amplitude.

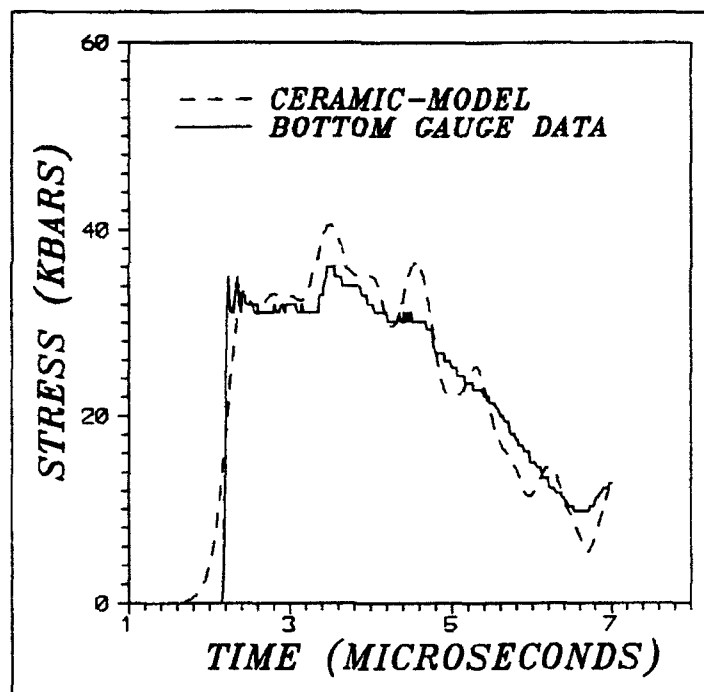


Figure 18. A comparison between the Rajendran-Grove ceramic model (with tensile  $n_1 = 0.1$ ) and bottom gauge data.

The results from these simulations indicate that the model prediction based on both brittle microcracking and plastic flow in the ceramic material matched the experimental measurements extremely well. The ceramic model not only matched the stress amplitude and the time duration, it also reproduced most of the salient features of the measured stress signal. The shade plots of damage also showed the experimentally observed fracture pattern such as the Hertzian cracks emanating from the edges of projectile-target interaction regions and the ceramic fracturing around the top gauge.

As a final exercise, the effect of interfaces between the target layers (top ceramic isodamp, isodamp bottom ceramic, and bottom ceramic aluminum) on the calculated stress history was investigated. Two cases were considered: (1) with slide lines between the layers, and (2) without any slide lines. In case (1) the interfaces are allowed to slip, and in case (2) interfaces are glued together so that no slip is allowed. The results from these two cases are compared in Figure 19.

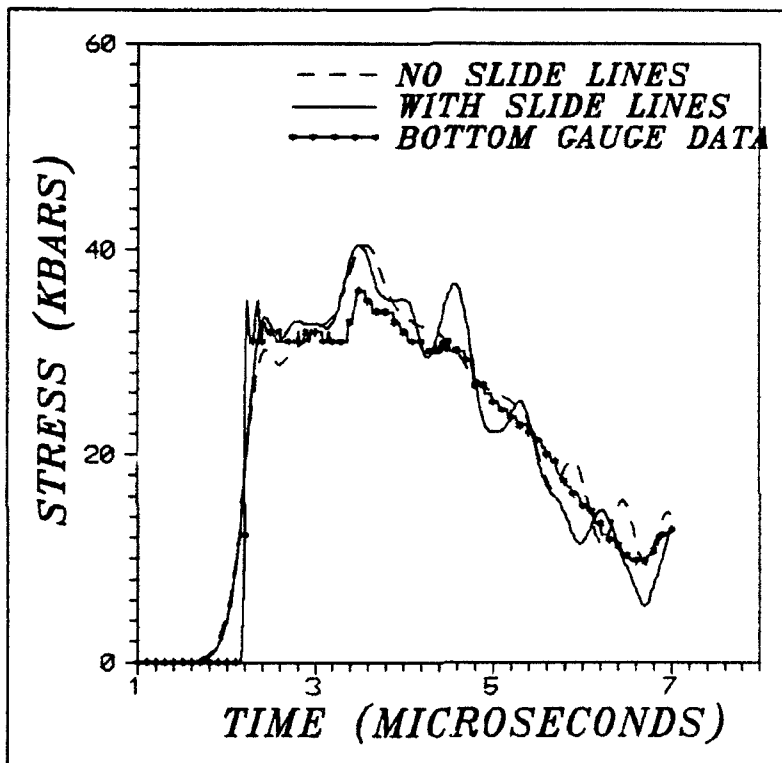


Figure 19. A comparison between stress histories for the cases with and without interface slide lines and the bottom gauge data.

The comparison plot in Figure 19 clearly shows that the calculated stress histories with and without slide lines produced similar results. This comparison demonstrates that the effect of interface sliding on the stress history is not significant, at least in the present application. However, the slide lines introduced some sort of (periodic) oscillations in the stress history during unloading. This may be due to the slide-line interaction introduced numerical noise. These results show that the influence of time step, mesh size, and slide line on the model calculated stress histories is minimum. Therefore, it may be concluded that the differences between the stress histories for the various cases are truly due to different types of material behaviors.



## Summary and Conclusions

### Summary

Recently, Rajendran [11] reported the development of an advanced ceramic model. This Rajendran-Grove ceramic model has been implemented into the 86 version of the EPIC-2 code and successfully used to model the impact behavior of AD85 ceramic under different impact test configurations such as the plane plate impact and rod-on-rod tests. The stress-strain states under these two configurations are fairly simple. In the plastic impact test, the strain is one-dimensional, and in the rod-on-rod test the stress is one-dimensional. There are seven model constants:  $K_{IC}$ ,  $\mu$ ,  $N_0^*$ ,  $a_0$ ,  $n_1^+$ ,  $n_1^-$ , and  $n_2$ . The fracture toughness value is taken from the fracture mechanics handbooks. The rest of the constants were determined from the experimental data. For this purpose, the manganin gauge measured stress histories from the plate impact and rod-on-rod impact experiments were employed.

The main objective of the present work is to demonstrate the applicability and generality of the Rajendran-Grove ceramic model under relatively complex stress-strain states. The idea is to employ the AD85 constants, determined from the plate impact and rod-on-rod impact tests data, to successfully describe the AD85 ceramic behavior under an entirely different experimental configuration. This report presented the ceramic model in detail and its successful application to describe the deformation and fracture in a layered ceramic target due to a steel projectile impact. The three-dimensional stress-strain state under this target configuration is fairly complex due to shock wave interactions. In the ballistic experiment, two manganin gauges were embedded in the target. This ballistic experiment was conducted by Vincent and Chang [18].

The 86 version of the EPIC-2 code was used to simulate the ballistic experiment. Several simulations were performed to understand and evaluate the effects of elastic, elastic-plastic, elastic-cracking, and elastic-plastic cracking behaviors on the measured stress histories. The results from the simulation in which the ceramic is assumed to behave fully elastically (without plastic flow and microcracking) did not match the data, whereas the elastic-plastic assumption produced reasonable results. The overall matching between the data and simulation was reasonably good. However, the details of the simulated wave profile did not agree with the experimentally measured stress profile. Similar results were observed when the ceramic was modeled as an elastic-microcracking solid without any plastic flow. These results showed that either the elastic-plastic or the elastic-cracking behavior was adequate to describe the impact behavior of ceramic. To verify the effects of a combined elastic-plastic cracking behavior on the stress history, the Rajendran-Grove ceramic model was employed in the ballistic experimental simulation.

In the simulation, the AD85 constants in Table 1 (with the exception of the tensile crack growth index constant,  $n_1^+$ ) were employed to describe the ceramic as an elastic-plastic microcracking material. The calculated stress history matched the measured stress history data extremely well. When a value of 1 was employed for  $n_1^+$ , the ceramic exhibited extensive damage and the simulated stress profile did not match with the experiment; however, a value of 0.1 for  $n_1^+$  predicted the data successfully. The Rajendran-Grove model also showed physically possible fracture patterns in the

ceramics. In summary, the ceramic model constants, estimated from the standard one-dimensional impact tests data, reproduced the multiaxial ballistic experimental data well.

### **Conclusions**

The inelastic deformations in ceramic materials due to impact loading, in general, consists of elastic, plastic, and microcracking components. It is not experimentally possible to isolate these deformations through any direct measurements. With lack of any recovery techniques to examine the post-impacted ceramic targets, especially at high velocity impact, only speculative assumptions can be made on the various deformation and fracture processes.

The computational analysis of the impact experiments using advanced ceramic models will indeed help in evaluating the various possible deformation and fracture modes in the ceramic materials. So far, the experimentalist have been making accurate velocity and stress measurements, high speed photographs, and X-ray radiographs. Interpretations and validations of these valuable measurements demand a detailed computational/analytical modeling of the impact experiments. These modeling efforts will eventually lead to a greater understanding of the impact behavior of ceramics.

In order to increase confidence in using the ceramic models as predictive tools in armor/antiarmor applications, generality of the model parameters should be tested using a variety of experimental data. The experiments should not only include various stress-strain states, but also a range of velocity regimes. Though the ballistic experiment could model well using the constants determined from one-dimensional experiments, the stress-strain state dependency on the tensile cracking requires additional investigation; therefore, the effects of the initial microflaw size and the number of microflaws on microcracking should be studied through additional simulations. In general, the continuum mechanics based, three-dimensional Rajendran-Grove ceramic model produced realistic results and matched a wide variety of experimental impact data.

### **Acknowledgments**

The author gratefully acknowledges the support of Alan Katz and Colin Freese of Computational Mechanics Group of Mechanics of Materials Division in installing and compiling the EPIC-2 code on an Apollo workstation. Colin Freese provided customized post-processors to plot and analyze the EPIC-2 numerical results. The author gratefully appreciates Dr. Shun-Chin Chou of the Materials Dynamics Branch for suggesting this project. Dr. Chou and Dr. Dandekar are also appreciated for their critical reviews of the manuscript.

## References

1. *Shock Compression of Condensed Matter - 1989 and Shock Compression of Condensed Matter - 1991*. Elsevier Science Publishers, B.V., 1990, 1992.
2. RAJENDRAN, A. M., and COOK, W. H. *A Comprehensive Review of Modeling of Impact Damage in Ceramics*. AFATL-TR-88-143, Eglin Air Force Base, FL, December 1988.
3. JOHNSON, G. R., and HOLMQUIST, T. J. *A Computational Constitutive Model for Brittle Materials Subjected to Large Strains, High Strain Rates, and High Pressures*. Shock Wave and High Strain Rates Phenomena in Materials, 1992.
4. JOHNSON, G. R., and COOK, W. H. *Fracture Characteristics of Three Metals Subjected to Various Strains, Strain Rates, Temperatures, and Pressures*. Eng. Fract. Mech, no. 21, 1985.
5. STEINBERG, D. J. *Computer Studies of the Dynamic Strength of Ceramics*. Shock Compression of Condensed Matter. Elsevier Science Publishers, B.V., 1992, p. 447-450.
6. GRADY, D. *Spall Strength of Condensed Matter*. J. Mech. Phys. Solids, v. 36, 1988, p. 353.
7. COCHRAN, S., and BANNER, D. *Spall Studies in Uranium*. J. Appl. Phys., v. 48, 1977, p. 2729.
8. ADDESSIO, F. L., and JOHNSON, J. N. *A Constitutive Model for the Dynamic Response of Brittle Materials*. LA-UR-89-2651, Los Alamos National Laboratory, Los Alamos, NM, 1989.
9. RAJENDRAN, A. M., and KROUPA, J. L. *Impact Damage Model for Ceramic Materials*. J. of Appl. Physics, v. 66, no. 8, 7-20, 1989, p. 3560-3565.
10. GRADY, D. E., and KIPP, M. E. *Continuum Modeling of Explosive Fracture in Oil Shales*. Int. J. Rock Mech. Min Sci. & Geomech., v. 17, 1980, p. 147-157.
11. RAJENDRAN, A. M. *High Strain Rate Behavior of Metals, Ceramics, and Concrete*. Air Force Report WL-TR-92-4006, Wright-Patterson Air Force Base, OH, April 1992.
12. GROVE, D. J., RAJENDRAN, A. M., BAR-ON, E., and BRAR, N. S. *Damage Evolution in a Ceramic Rod*. Shock Compression of Condensed Matter - 1991. S. C. Schmidt, et al., eds., Elsevier Science Publishers, 1992, p. 971-975.
13. RAJENDRAN, A. M., DIETENBERGER, M. A., and GROVE, D. J. *Microphysical Model to Describe Impact Behavior of Ceramics*. Constitutive Laws for Engineering Materials, C. S. Desai, et al., eds., ASME Press, 1991, p. 609.
14. RAJENDRAN, A. M., and GROVE, D. J. *Modeling the Impact Behavior of AD85*. 24th Int. SAMPE Tech. Conf. Proceedings, Allied-Signal, Inc., Publishers, October 1992.
15. MARGOLIN, L. G. *Elastic Moduli of a Cracked Body*. Int. Journal of Fracture, v. 22, 1983, p. 65-79.
16. GURSON, A. L. *Porous Rigid-Plastic Materials Containing Rigid Inclusions - Yield Function, Plastic Potential, and Void Nucleation*. Adv. Res. Strength Fract. Matls., 2a, D. M. R. Tablin, ed., Pergamon Press, NY, 1977.
17. JOHNSON, G. R., and STRYK, R. A. *User Instructions for the EPIC-2 Code*. AFATL-TR-86-51, Eglin Air Force Base, FL, 1986.
18. VINCENT, P. M., and CHANG, A. L. *Ballistic Impact Pressure Pulse Measurement*. Presented at 41st Meeting of Aeroballistic Range Association, October 22-25, 1990.
19. MARGOLIN, L. G. *Microphysical Models for Inelastic Material Response*. International Journal of Engineering Science, v. 8-10, no. 22, 1984, p. 1171-1179.
20. BUDIANSKY, B., and O'CONNELL, R. J. *Elastic Moduli of a Cracked Solid*. Int. J. of Solids and Structures, v. 12, 1976, p. 81-97.
21. MACKENZIE, J. H. *The Elastic Contents of a Solid Containing Spherical Holes*. Proc. Phys. Soc., v. 2, no. 63, 1950.
22. JOHNSON, J. N. *Dynamic Fracture and Spallation in Ductile Solids*. J. Appl. Phys. v. 52, no. 4, 1981, p. 2812.
23. GRIFFITH, A. A. *The Phenomena of Rupture and Flow in Solids*. Phil. Trans. of Royal Soc. of London, v. 221, 1920, p. 163-198.

24. MARGOLIN, L. G. *A Generalized Griffith Criterion for Crack Propagation*. Engineering Fracture Mechanics, v. 19, v. 30, 1984, p. 539-543.
25. DIENES, J. K. *Comments on 'A Generalized Griffith Criterion for Crack Propagation' by L. G. Margolin*. A Technical Note, Eng. Fracture Mechanics, v. 3, no. 23, p. 615-617.
26. JOHN, R. *Mixed Mode Fracture of Concrete Subjected to Impact Loading*. PhD Thesis, Northwestern University, Evanston, IL, 1988.
27. KANNINEN, M. F., and POPELAR, C. H. *Advanced Fracture Mechanics*. Oxford University Press. New York, NY, 1985.
28. DANDEKAR, D. P., and HANKIN, M. *Deformation of a Polyvinyl Based Elastomer Subjected to Shock Loading*. Shock Compression of Condensed Matter - 1989, Elsevier Science, 1990, p. 97.

## Appendix

### Degraded Moduli Expressions

Margolin [15] derived the degraded elastic moduli for noninteracting, penny-shaped microcracks of various sizes and in random orientations and the corresponding expressions for the isotropic elastic moduli,  $C_{ijkl}$  in Equation 3 are:

$$C_{ijkl} = C_1 \delta_{ik} \delta_{jl} + C_2 \delta_{ik} \delta_{jl} + C_3 \delta_{ik} \delta_{jl} , \quad (19)$$

where

$$C_1 = B_0 + \frac{1}{4G} , \quad (20)$$

$$C_2 = D_0 + \frac{1}{4G} , \quad (21)$$

and

$$C_3 = A_0 - \frac{\nu}{2(1+\nu)G} . \quad (22)$$

In the above equations,  $G$  and  $\nu$  are the shear modulus and Poisson's ratio, respectively, of the undamaged material while  $A_0$ ,  $B_0$ , and  $D_0$  are damage parameters whose values depend on the stress state. To evaluate these parameters, Margolin defined a microcrack density parameter,

$$\gamma_0^* = \frac{16N_o^* a_{\max}^3}{45 E} . \quad (23)$$

In Equation 23,  $\gamma_0^*$  is the microcrack density and  $E$  is the Young's modulus of the undamaged material.  $N_o^*$  is the number of microcracks per unit volume, and  $a_{\max}$  is the maximum microcrack size. Margolin identified the following four cases of stress state in evaluating the damage parameters  $A_0$ ,  $B_0$ , and  $D_0$ :

Case 1:  $\bar{\sigma}_1, \bar{\sigma}_2, \bar{\sigma}_3 > 0$   
(all principal stresses are tensile)

$$A_0 = \left[ (1 - \nu^2) - (1 + \nu) \right] \gamma^* \quad (24)$$

$$B_0 = \left[ (1 - \nu^2) + 4(1 + \nu) \right] \gamma^* \quad (25)$$

$$D_0 = A_0 \quad (26)$$

Case 2:  $\bar{\sigma}_1, \bar{\sigma}_2, \bar{\sigma}_3 < 0$   
(all principal stresses are compressive)

$$A_0 = -(1 + \nu) \gamma^* \quad (27)$$

$$B_0 = 4(1 + \nu) \gamma^* \quad (28)$$

$$D_0 = A_0 \quad (29)$$

Equations 27 through 29 will result in the degradation of the shear modulus, but not of the bulk modulus because under compression only crack movement of the closed microcracks under modes II and III are permitted.

Case 3:  $\bar{\sigma}_1, \bar{\sigma}_2, > 0, \bar{\sigma}_3 < 0$   
(two principal stresses are tensile and one principal stress is compressive)

$$A_0 = \left[ \frac{(5\beta^3 - 3\beta^5)}{2} (1 - \nu^2) - (1 + \nu) \right] \gamma^* \quad (30)$$

$$B_0 = \left[ \frac{(5\beta^3 - 3\beta^5)}{2} (1 - \nu^2) + 4(1 + \nu) \right] \gamma^* \quad (31)$$

$$D_0 = \left[ (6\beta^5 - 5\beta^3) (1 - \nu^2) - (1 + \nu) \right] \gamma^* \quad (32)$$

where

$$\beta \approx \sqrt{\frac{\bar{\sigma}_1 + \bar{\sigma}_2}{\bar{\sigma}_1 + \bar{\sigma}_2 - 2\bar{\sigma}_3}} \quad (33)$$

Case 4:  $\bar{\sigma}_1 > 0, \bar{\sigma}_2, \bar{\sigma}_3 < 0$   
(one principal stress is tensile and two principal stresses are compressive)

$$A_0 = \left[ \frac{5(1-\beta^3) - 3(1-\beta^5)}{2} (1-\nu^2) - (1+\nu) \right] \gamma^* \quad (34)$$

$$B_0 = \left[ \frac{5(1-\beta^3) - 3(1-\beta^5)}{2} (1-\nu^2) + 4(1+\nu) \right] \gamma^* \quad (35)$$

$$D_0 = \left\{ \left[ 6(1-\beta^5) - 5(1-\beta^3) \right] (1-\nu^2) - (1+\nu) \right\} \gamma^* \quad (36)$$

where

$$\beta \approx \sqrt{\frac{\bar{\sigma}_2 + \bar{\sigma}_3}{\bar{\sigma}_2 + \bar{\sigma}_3 - 2\bar{\sigma}_1}} \quad (37)$$

In the Rajendran-Grove ceramic model, the compliance tensor  $C$  is analytically inverted to the stiffness tensor  $M$  using the following identity relationship:

$$M_{ijkl} C_{ijkl} = \frac{(\delta_{ik} \delta_{jl} + \delta_{il} \delta_{jk})}{2} ; \quad (38)$$

a relationship can be established between  $C_1$ ,  $C_2$ , and  $C_3$  of Equation 20 through 22 and  $m_1$ ,  $m_2$ , and  $m_3$  of the following relationship:

$$M_{ijkl} = m_1 \delta_{ik} \delta_{jl} + m_2 \delta_{il} \delta_{jk} + m_3 \delta_{ij} \delta_{kl} , \quad (39)$$

where

$$m_1 = m_2 = \frac{1}{2(C_1 + C_2)} \quad (40)$$

and

$$m_3 = \frac{-C_3}{(C_1 + C_2)(C_1 + C_2 + 3C_3)} \quad (41)$$

The effective degraded shear and bulk moduli are defined as

$$\bar{G} = m_1 \quad (42)$$

and

$$\bar{K} = m_3 + \frac{2}{3} m_1 \quad (43)$$

Instead of employing the Margolin's expression for Case 1 (all principal stresses are tensile), the Budiansky and O'Connell [20] solutions can be used for randomly oriented, noninteracting microcracks under tensile loading. The corresponding relationships for the damaged stiffness solutions are:

$$m_1 = m_2 = \bar{G} \quad (44)$$

$$m_3 = \frac{2 \bar{G} \bar{\nu}}{(1 - 2 \bar{\nu})} \quad (45)$$

where

$$\bar{\nu} = \nu \left( 1 - \frac{16}{9} \gamma \right) \quad (46)$$

and

$$\bar{G} = G \left\{ 1 - \left( \frac{32}{45} \right) \frac{(1 - \bar{\nu})(5 - \bar{\nu})}{(2 - \bar{\nu})} \gamma \right\} \quad (47)$$

In these equations,  $\bar{\nu}$  and  $\bar{G}$  are the Poisson's ratio and shear modulus, respectively, of the microcrack damaged material. Using  $m_1$  and  $m_3$  from Equations 44 and 45, the degraded bulk modulus can be computed from Equation 43. It is obvious from Equations 44 through 47 that a complete loss of strength is predicted when the microcrack density  $\gamma$  reaches 9/16. For tensile loading conditions, based on the comparison with Margolin's equations, there is no bound on the crack density. However, Budiansky and O'Connell's solution limits the crack density to 9/16. This permits the damage parameter to vary from zero (no damage) to one (fully damaged). Therefore, in the ceramic model, Budiansky and O'Connell's equations are used instead of Margolin's equations for the case when all the principal stresses are positive (see Case 1).



# DISTRIBUTION LIST

No. of Copies	To
1	Office of the Under Secretary of Defense for Research and Engineering, The Pentagon, Washington, DC 20301
	Director, U.S. Army Research Laboratory, 2800 Powder Mill Road, Adelphi, MD 20783-1197
1	ATTN: AMSRL-OP-CI-AD, Technical Publishing Branch
1	AMSRL-OP-C.-AD, Records Management Administrator
1	AMSRL-SS
	Commander, Defense Technical Information Center, Cameron Station, Building 5, 5010 Duke Street, Alexandria, VA 22304-6145
2	ATTN: DTIC-FDAC
1	MIA/CINDAS, Purdue University, 2595 Yeager Road, West Lafayette, IN 47905
	Commander, Army Research Office, P.O. Box 12211, Research Triangle Park, NC 27709-2211
1	ATTN: Information Processing Office
1	Andrew Crowson
1	Dr. Kailasam Iyler
	Commander, U.S. Army Materiel Command, 5001 Eisenhower Avenue, Alexandria, VA 22333
1	ATTN: AMCSCI
	Commander, U.S. Army Materiel Systems Analysis Activity, Aberdeen Proving Ground, MD 21005
1	ATTN: AMXSY-MP, H. Cohen
	Commander, U.S. Army Missile Command, Redstone Arsenal, AL 35809
1	ATTN: AMSMI-RD-CS-R/Doc
	Commander, U.S. Army Armament, Munitions and Chemical Command, Dover, NJ 07801
2	ATTN: Technical Library
	Commander, U.S. Army Natick Research, Development and Engineering Center, Natick, MA 01760-5010
1	ATTN: Technical Library
	Commander, U.S. Army Satellite Communications Agency, Fort Monmouth, NJ 07703
1	ATTN: Technical Document Center
	Commander, U.S. Army Tank-Automotive Command, Warren, MI 48397-5000
1	ATTN: AMSTA-ZSK
1	AMSTA-TSL, Technical Library
1	AMSTA-RSK, Samuel Goodman
	Commander, White Sands Missile Range, NM 88002
1	ATTN: STEWS-WS-VT
	President, Airborne, Electronics and Special Warfare Board, Fort Bragg, NC 28307
1	ATTN: Library
	Director, U.S. Army Research Laboratory, Aberdeen Proving Ground, MD 21005-5066
1	ATTN: AMSRL-WT
1	William Gooch
1	George Hauver, AMSRL-WT-TA
1	Michael J. Scheidler, AMSRL-WT-TD
1	AMSRL-TB-W
1	AMSRL-TB-AM
1	AMSRL-TB-P
1	AMSRL-AMB-TBD
	Commander, Dugway Proving Ground, UT 84022
1	ATTN: Technical Library, Technical Information Division

No. of Copies	To
1	NASA - Langley Research Center, Hampton, VA 23665-5225 U.S. Army Vehicle Propulsion Directorate, NASA Lewis Research Center, 2100 Brookpark Road, Cleveland, OH 44135-3191 ATTN: AMSRL-VP
1	NASA - Lewis Research Center, 2100 Brookpark Road, Cleveland, OH 44135-3191 Director, Defense Intelligence Agency, Washington, DC 20340-6053 ATTN: ODT-5A (Mr. Frank Jaeger)
1	Air Force Armament Laboratory, Eglin Air Force Base, FL 32542-5434 ATTN: J. C. Foster, Jr. W. H. Cook
1	Naval Post Graduate School, Monterey, CA 93943 ATTN: Joseph Sternberg, Code EW Lawrence Livermore National Laboratory, Livermore, CA 94550 ATTN: J. E. Reaugh, L-290 R. L. Landingham, MC L-369 Dr. M. Finger, L-38 Daniel J. Steinberg Carl R. Cline
1	Naval Surface Warfare Center, Silver Spring, MD 20903-5000 ATTN: F. J. Zerilli, Code R13 Naval Surface Warfare Center, Dahlgren, VA 22448 ATTN: William H. Holt, Naval Code G35 Los Alamos National Laboratory, Los Alamos, NM 87545 ATTN: Mike Burkett J. Repa, DRA-CDT, MS F668 J.W. Straight, M-8, MS J960 R. Karpp, M-8, J960 J. Taylor, ADDRA, MS A110 Dr. P. S. Follansbee, MST-5, MS G730 Dr. J. N. Johnson, T-14, MSB214 Dr. P. J. Mauldin, N-6, MS K557 Dr. F. Adessio, T-3, MS B216 Thomas F. Adams, X-3, MS F663 G. E. Cort, ATAC, MS, K574 Denise Hunter Dave Mandell Samuel R. Skaggs Anna Zurek Dr. B. M. Hogan
1	Southwest Research Institute, 6220 Culebra Road, San Antonio, TX 78238 ATTN: James Lankford Dr. C. E. Anderson David Littlefield
1	Southwest Research International, 333 Ravenwood Avenue, Menlo Park, CA 94025 ATTN: Richard Klopp Institute for Defense Analysis, 1801 N. Beauregard Street, Alexandria, VA 22311-1772 ATTN: Dr. George Mayer Dr. Marc A. Adams, JPL MS 97-B, 4800 Oak Grove Drive, Pasadena, CA 91109 P.D. Buckley, NMIMT, TERA Group, Socorro, NM 87801 California Institute of Technology, Geophysics Division MS/252-21, Pasadena, CA 91125 ATTN: Professor T. J. Ahrens

No. of Copies	To
	Director, Benet Weapons Laboratory, LCWSL, USA AMCCOM, Watervliet, NY 12189
1	ATTN: AMSMC-LCB-TL
1	AMSMC-LCB-R
1	AMSMC-LCB-RM
1	AMSMC-LCB-RP
1	AMSMC-TB-AM, G. Randers-Pehrson
1	AMSMC-TB-P, S. Segletes
1	AMSMC-AMB-TBD, K. Kimsey
1	AMSMC-TB-W, Thomas W. Wright
	Commander, U.S. Army Foreign Science and Technology Center, 220 7th Street, N.E., Charlottesville, VA 22901-5396
3	ATTN: AIFRTC, Applied Technologies Branch, Gerald Schlesinger
	Commander, U.S. Army Aeromedical Research Unit, P.O. Box 577, Fort Rucker, AL 36360
1	ATTN: Technical Library
	U.S. Army Aviation Training Library, Fort Rucker, AL 36360
1	ATTN: Building 5906-5907
	Commander, U.S. Army Agency for Aviation Safety, Fort Rucker, AL 36362
1	ATTN: Technical Library
	Commander, Clarke Engineer School Library, 3202 Nebraska Ave., N. Ft. Leonard Wood, MO 65473-5000
1	ATTN: Library
	Commander, U.S. Army Engineer Waterways Experiment Station, P.O. Box 631, Vicksburg, MS 39180
1	ATTN: Research Center Library
	Commandant, U.S. Army Quartermaster School, Fort Lee, VA 23801
1	ATTN: Quartermaster School Library
	Naval Research Laboratory, Washington, DC 20375
2	ATTN: Dr. G. R. Yoder - Code 6384
	Chief of Naval Research, Arlington, VA 22217
1	ATTN: Code 471
	Commander, U.S. Air Force Wright Research & Development Center, Wright-Patterson Air Force Base, OH 45433-6523
1	ATTN: WRDC/MLLP, M. Forney, Jr.
1	WRDC/MLBC, Mr. Stanley Schulman
	NASA - Marshall Space Flight Center, MSFC, AL 35812
1	ATTN: Mr. Paul Schuerer/EH01
	U.S. Department of Commerce, National Institute of Standards and Technology, Gaithersburg, MD 20899
1	ATTN: Stephen M. Hsu, Chief, Ceramics Division, Institute for Materials Science and Engineering
	Committee on Marine Structures, Marine Board, National Research Council, 2101 Constitution Avenue, N.W., Washington, DC 20418
1	Materials Sciences Corporation, Suite 250, 500 Office Center Drive, Fort Washington, PA 19034
1	Charles Stark Draper Laboratory, 555 Technology Square, Cambridge, MA 02139
	Wyman-Gordon Company, Worcester, MA 01601
1	ATTN: Technical Library
	General Dynamics, Convair Aerospace Division P.O. Box 748, Fort Worth, TX 76101
1	ATTN: Mfg. Engineering Technical Library
	Plastics Technical Evaluation Center, PLASTEC, ARDEC Bldg. 355N, Picatinny Arsenal, NJ 07806-5000
1	ATTN: Harry Peibly
	Department of the Army, Aerostructures Directorate, MS-266, U.S. Army Aviation R&T Activity - AVSCOM, Langley Research Center, Hampton, VA 23665-5225
1	Department of the Army, Armament Research and Development Center, Dover, NJ 07801
1	ATTN: Dr. E. Bloore

No. of Copies	To
1	GTE Products Corporation, Towanda, PA 18848 ATTN: Jeff Gonzalez
1	RARDE, Fort Halstead - Sevenoaks, TN14 7BP Kent, England ATTN: Dr. Phillip Church
1	Department of FV&S7, DRA (Chertsey), Chobham Lane, Chertsey, Surrey, England ATTN: Dr. Anthony Hawkins
1	National Defense Research Establishment, Box 27322, S-102 54 Stockholm, Sweden ATTN: Dr. Per-Olof Olsson
1	Brown University, Division of Engineering, 182 Hope Street, Providence, RI 02912 ATTN: Ben Freund
1	California Research & Technology, Inc., 5117 Johnson Drive, Pleasanton, CA 94566 ATTN: Dennis L. Orphal
1	The Carborundum Company, P.O. Box 1054, Niagra Falls, NY 19302 ATTN: Robert Palia
1	Alme and Associates, 9650 Santiago Road STE 102, Columbia, MD 21045 ATTN: Marvin L. Alme
1	Institute for Advanced Technology, 4030-2 West Braker, Austin, TX 78759-5329 ATTN: Stephan Bless
1	University of Dayton Research Institute, KLA14, 300 College Park, Dayton, OH 45469-0182 ATTN: N. Singh Brar
1	University of Dayton, Building JPC 201, Dayton, OH 45469 ATTN: Mr. David J. Grove
1	General Dynamic, Land Systems Division, P.O. Box 1800, Warren, MI 48090 ATTN: Wayne A. Burke
1	General Research Corporation, 5383 Hollister Avenue, Santa Barbara, CA 93160-6770 ATTN: Alex Charters
1	T. L. Menna
1	Sandia National Laboratories, P.O. Box 5800, Albuquerque, NM 87185 ATTN: Peter Chen
1	Dr. Dennis E. Grady, ORG 1533
1	Jack L. Wise
1	The Pentagon, ODDR&E, Washington, DC 20305 ATTN: W. E. Snowden
1	DARPA/Materials Science Office, 1400 Wilson Boulevard, Arlington, VA 22209-2308 ATTN: B. Wilcox
1	Trans Science Corporation, P.O. Box 2727, La Jolla, CA 92038 ATTN: G. A. Hegemier
1	The University Of Texas at Austin, Austin, TX 78712 ATTN: Eric Farenthold, Department of Mechanical Engineering
1	Michael Marder, Department of Physics, RLM 14.212
1	Steve Gross, Center for Non-Linear Dynamics, RLM14
1	Ching-Hsie Yew, Aerospace Engineering Department, WRW 316B
1	Ahmed Shaaban, Aerospace Engineering Department, WRW 316B
1	Chadee Persad, Institute for Advanced Technology
1	Purdue University, School of Aeronautics & Astronautics, West Lafayette, IN 47907 ATTN: Horacio D. Espinosa

No of Copies	To
	University of California - San Diego, Department of Applied Mechanics & Engineering Services R011, La Jolla, CA 92093-0411
1	ATTN: Sia Nemat-Nasser
	DARPA/TTO, 3701 North Fairfax Drive, Arlington, VA 22203-1714
1	ATTN: Robert Kocher
	Lanxide Armor Products, Inc., 1300 Marrows Road, P.O. Box 6077, Newark, DE 19714-6077
1	ATTN: Katherine T. Leighton
	University of Hawaii at Manoa, Mineral Physics Group, Department of Geology & Geophysics, 225 Correa Road, Honolulu, HI 96822
1	ATTN: Murli Manghnani
	Michigan Technical University, Department of Mechanical Engineering, 1400 Townsend Drive, Houghton, MI 49931-1295
1	ATTN: Bill Predebon
	Kaman Sciences Corporation, P.O. Box 7463, 1500 Garden of the Gods Road, Colorado Springs, CO 80933
1	ATTN: Dr. Michael J. Normandia
	Cercom, 1950 Watson Way, Vista, CA 92083
1	ATTN: Rich Palicka
	Poulter Laboratory, SRI International, 333 Ravenswood Avenue, Menlo Park, CA 94025
1	ATTN: Dr. Donald Curran
1	Lynn Seaman
1	Don A. Shockey
1	Dr. Robert D. Caligiuri
	Alliant Techsystems, Inc., 7225 Northland Drive, Brooklyn Park, MN 55428-1515
1	ATTN: T. J. Holmquist
1	Dr. Gordon R. Johnson
	E.I. Du Pont De Nemours & Company, Wilmington, DE 19898
1	ATTN: Dr. Barry E. Bowen
	California Research & Technology, Inc., 5771 Johnson Drive, Pleasanton, CA 94566
1	ATTN: Dr. Ronald E. Brown
	Aeronautical Research Associates of Princeton, Inc., 50 Washington Road, P.O. Box 2229 Princeton, NJ 08540
1	ATTN: Dr. Ross M. Contiliano
	Dow Chemical Company, Midland, MI 48640
1	ATTN: Mr. Kenneth O. Groves
	Director, U.S. Army Research Laboratory, Watertown, MA 02172-0001
2	ATTN: AMSRL-OP-CI-D, Technical Library
5	Author